Table of Contents

List of Figures

List of Tables

Chapter # 1

Introduction

1.1 Energy

Due to the rise in energy demand, the globe is moving closer and closer to a serious power crisis [1]. Due to its expanding population and weak long-term planning for its energy-based infrastructure, Pakistan is currently experiencing its biggest energy crisis [2,3]. The installation of thermal power plants has largely served as the focus for short-term solutions [2]. Fossil fuels are imported into Pakistan for usage in thermal power plants, which use them to generate electricity. Energy generated from imported fuel is an incredibly costly solution for a growing country like Pakistan [4]. Nuclear power facilities have also been built; however, they have limited capacity [5]. The potential environmental risk posed by these thermal power facilities is also disregarded. Pakistan's primary energy production sources are oil (35.20%), hydel (29.90%), natural gas (29.00%), nuclear energy (5.70%), and imported energy. The average annual energy consumption in Pakistan is 17,000 MW, while there is now a 400–5000 MW shortage. It is expected that within the next ten years the demand for energy might increase by 4-5%, or around 1500 MW [6]. It is not environmentally good to use fossil fuels, especially carbon, to generate electricity. On the other hand, environmentally friendly renewable energy sources provide a more affordable solution as shown in fig. 1.1 [7, 8]. With the utilization of renewable energy sources, Pakistan must overcome problems in its energy planning [9]. Therefore, in addition to concentrating on these standard energy sources, fuel cell (FC) technology should be used to investigate non-traditional energy sources such as solar, hydrogen, geothermal, wind, tidal power, and biomass [10, 11]. No other energy generating method can compare to the advantages provided by FC technology [12].

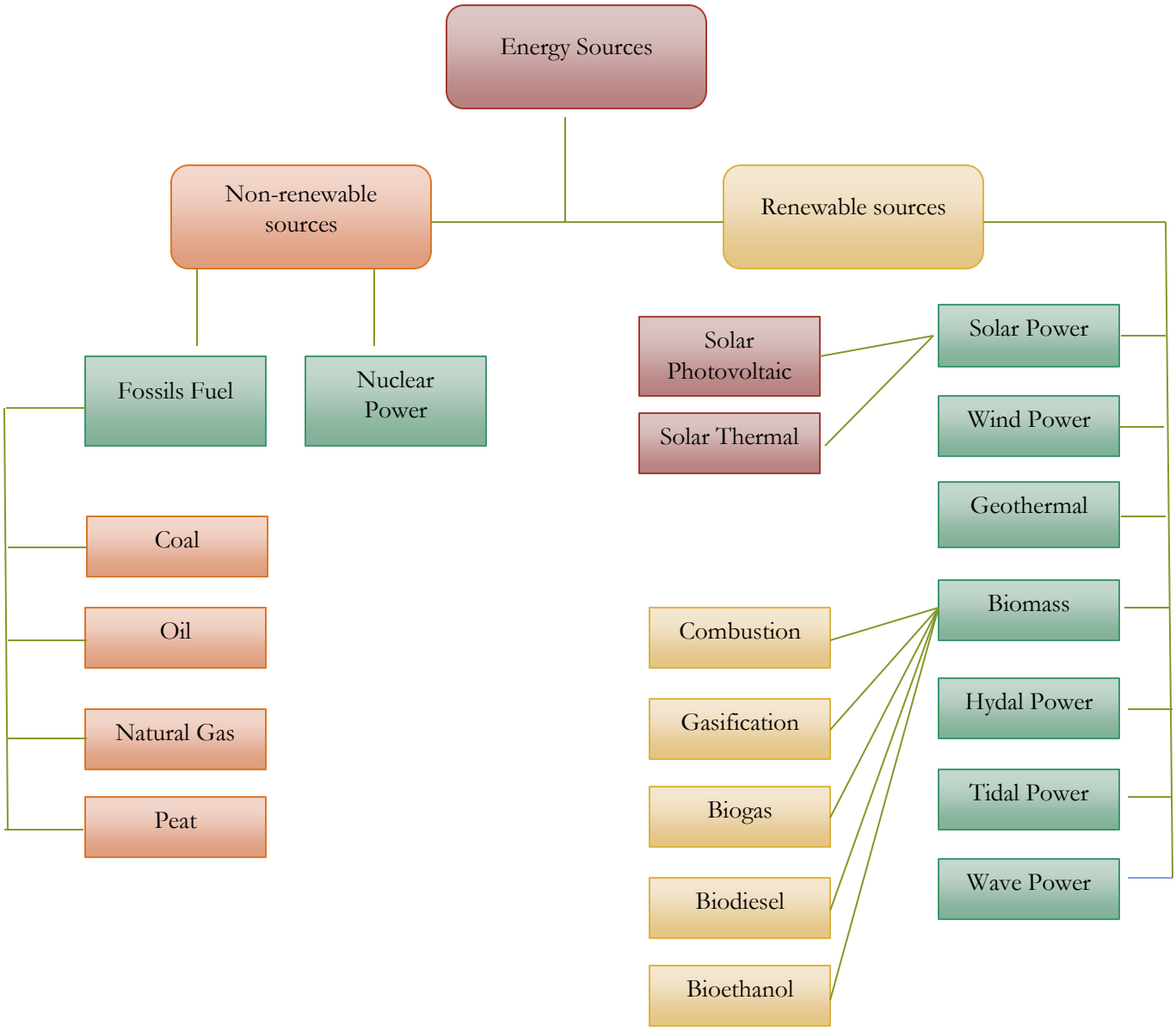

Figure 1.1 The types of energy resources that are present in Pakistan [13].

14% of energy used in the world comes from sources that can be replenished [14]. It covers biomass, geothermal, solar, wind, and hydrothermal energy. These energy sources are fundamental, domestic, clean, or limitless as shown in fig. 1.2 [15, 16]. These technologies have the problem that they depend on nature and do not meet global energy demands [17]. Demands for energy have been steadily rising as the population has grown and as the social economy has improved. As a result, it's crucial to support an energy-efficient, secure, and clean electrical energy generator. Researchers and modern analysts have highlighted out SOFCs among other power devices for their adaptable fills, high energy transformation productivity, as well as their low carbon byproduct and ability to meet energy demands at an industrial level, which is a major demand of developed countries [18–25].

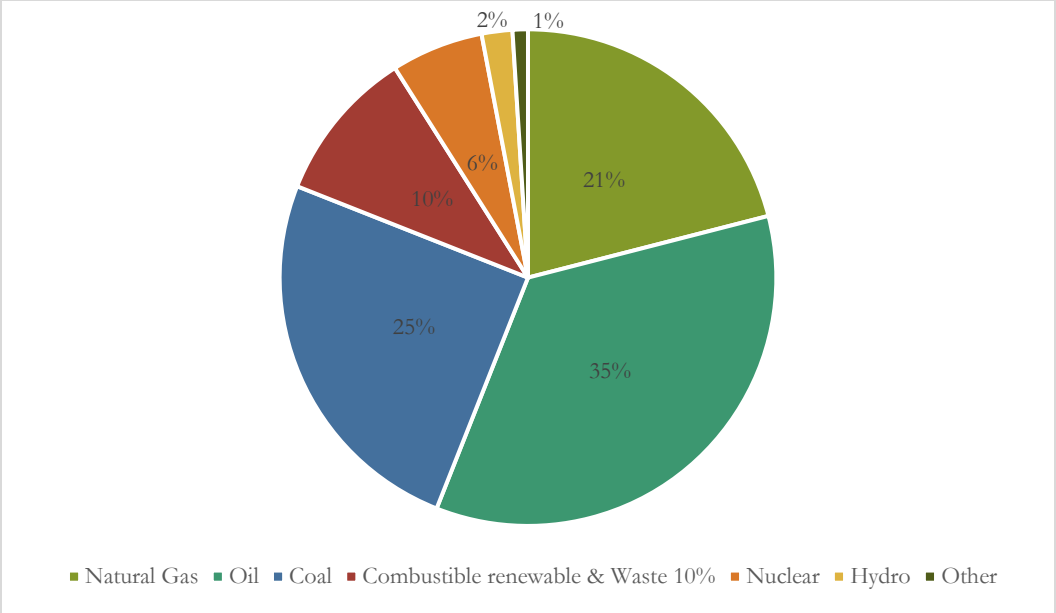

Figure 1.2 Sustainable energy for developing countries

1.2 Fuel Cell

In 1838, chemist Sir William Grove created the first fuel cell while experimenting with electrolysis of water. Water may electrolyze into hydrogen and oxygen whenever an electric current is applied to it. By combining hydrogen and oxygen, he was able to generate an electric current, which he then measured with an ammeter instead of a battery. William Grove is credited with developing the fuel cell. After working on large fuel cell system for a while in 1895, Jacques was able to produce 1.5kW stacks using a significant number of fuel cells. Due to this achievement, the fuel cell device can now generate 30 kilowatts of electricity.

An effective method of converting chemical energy into electrical energy without burning is using fuel cells. The cathode employs an oxidizer, while the anode uses an external fuel. When there is an electrolyte present, this reaction continues. The reagent is introduced into the electrolytic cell, all equipment is turned off, but electricity is still present [26].

1.2.1 Reactions in fuel cell

At anode

In the prescience of catalyst and hydrogen fuel, Oxidation occurs, and protons and electrons are formed.

$2H_2 \rightarrow 4H^+ + 4e^-$ **(1)**

At Cathode

The Formation of water as chemical reaction occur with oxygen when electrons and protons interact as shown.

$O_2 + 4H^+ \rightarrow 2H_2O$ **(2)**

Net Reaction

$2H_2 + O_2 \rightarrow 2H_2O$ **(3)**

1.3 Fuel cell types

Depending on the electrolyte and fuel used, multiple types of fuel cells can be identified.

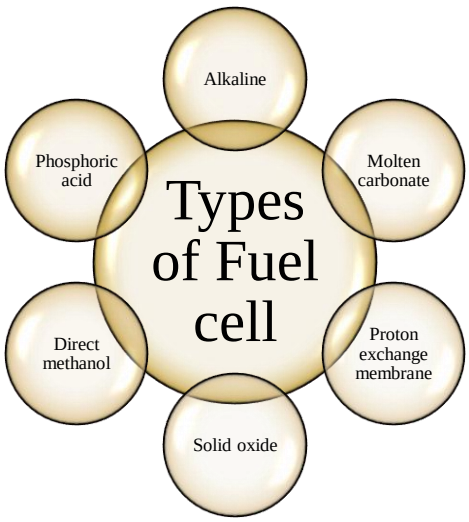

1.3.1 Alkaline fuel cell (AFC)

AFCs operate between temperature range of 100°C and 250°C, or between 212°F and 482°F. However, newer AFC designs function at temperatures that are typically between 74- and 158-degrees Fahrenheit, or 23 to 70 degrees Celsius.

Because of the speed at which substance responses take place inside the cell, AFCs have good power densities. They are also extremely productive, with a space application efficiency of between 50% and 60% [27].

Anode-side reaction

$$H_2 + 4OH^- \longrightarrow 4e^- + 4H_2O \quad \textbf{(4)}$$

Cathode-side reaction

$$O_2 + 2H_2O + 4e^- \longrightarrow 4OH^- \quad \textbf{(5)}$$

1.3.2 Molten-carbonate fuel cell

The carbonates energy components use molten sodium carbonate as the fuel cell's electrolyte. Methane or gaseous gasoline can be used as fuel, which are hydrocarbon gases. These power sources, often known as fuel cells, have an efficiency range of 55–60% or higher.

Negative particles pass into electrolyte and travel to the anode side of molten carbonate energy components where water is created by their fusion with hydrogen and a significant number of electrons [28].

Anode-side reaction

$$CO_3^{2-} + H_2 \longrightarrow H_2O + CO_2 + 2e^- \quad \textbf{(6)}$$

$$CO + CO_3^{2-} \longrightarrow 2e^- + 2CO_2 \quad \textbf{(7)}$$

$CH_4 + CO_3^{2-} \longrightarrow 5CO_2+2H_2O+8e^-$ **(8)**

Cathode-side reaction

$1/2\ O_2 + 2\ CO_2+ 2e^- \longrightarrow CO_3^{2-}$ **(9)**

1.3.3 Phosphorus acid fuel cell (PAFC)

Anode, cathode, and electrolyte are the three layers that make up phosphoric acid (PA) fuel cells, another type. The catalyst used to make the cathode and anode is platinum, which are constructed of carbon and another structure made of silicon carbide that transports the electrolyte using phosphoric acid. Protons move from anode side to cathode side of fuel cell with phosphoric acid electrolyte, where they combine with oxygen and electrons to produce heat and water. The working temperature range for this fuel cell is 160 to 220 °C, and its power range is 10 kW to 1 MW [29].

Anode-side reaction

$2H + H_2 \longrightarrow 2e^-$ **(10)**

Cathode-side reaction

$2H^+ + 1/2\ O_2 + 2e^- \longrightarrow H_2O$ **(11)**

1.3.4 Proton-exchange membrane fuel cell (PEMFC)

The electrolyte substance in PEMFC is a solid polymer. Its operating range is between 30 and 100 °C. Carbon-supported Pt serves as both a cathode and an anode. H_2 is used as an oxidant or as fuel. Its range of power is 1W to 100 kW.

Anode-side reaction

$H_2 \longrightarrow 2e^- + 2H^+$ **(12)**

Cathode-side reaction

$2H^+ + 1/2\ O_2 + 2e^- \longrightarrow H_2O$ **(13)**

Table 1.1: Characteristics comparison of different types of Fuel cells [30]

Fuel cell	Electrolyte	Operating Temperature	Electrical Efficiency	Fuel
Alkaline Fuel cell (AFC)	KOH solutions	Room temperature to 90°C	60-70%	H_2-O_2
Proton exchange membrane fuel cell (PEMFC)	Proton exchange membrane	Room temperature to 80°C	40-60%	H_2-O_2 or air
Direct methanol fuel cell (DMFC)	Proton exchange membrane	Room temperature to 130°C	20-30%	CH_2H_2-O_2 or air
Phosphoric acid fuel cell (PAFC)	Phosphoric acid	160-220°C	55%	Natural gas, biogas, H_2-O_2 or air
Molten carbonate fuel cell (MCFC)	Molten mixture of alkali metal carbonate	620-660°C	65%	Natural gas, biogas, coal gas H_2-O_2 or air
Solid oxide fuel cell (SOFC)	Oxide ion conducting ceramics	800-1000°C	60-655%	Natural gas, biogas, coal gas H_2-O_2 or air

1.4 Solid oxide fuel cell technology

In SOFC, which is device for turning energy into electricity, fuel and an oxidant are electrochemically mixed over an ionic conducting oxide electrolyte. The anode and cathode, two porous electrodes, sandwiched by the dense electrolyte; this arrangement of electrodes is referred to as a single cell. Fuel is delivered to the anode, where it undergoes an oxidation reaction and releases electrons into the external circuit. The cathode receives oxidant, which then goes through a reduction process and takes electrons from the external circuit. Direct current electricity is

created when an electron travels from the anode to the cathode of the external circuit. A component known as the connector, which is seen in Fig. 1, is used to electrically connect single cells in a SOFC stack in series.

The most popular materials for SOFCs right now are nickel/YSZ for the anode, strontium-doped lanthanum manganite (LSM) for cathode, oxide ion conducting yttria-stabilized zirconia (YSZ) for electrolyte, and metals with a high melting point for the connection. Depending on exact cell configurations and system designs, SOFC runs between 700 and 1000 °C in air or pressurized settings. The SOFC has gotten a lot of interest recently, and development work in this field has increased dramatically [30-33]. It is appealing because SOFC technology efficiently produces energy from a variety of fuels for a wide range of power production applications.

1.4.1 SOFC components

The cathode, anode and electrolyte are the three essential components of a solid oxide fuel cell. An assembly of membrane electrodes has three layers as shown in fig. 1.3. Approximately 1V and 1W/cm2 of voltage and electricity are generated by a single fuel cell. As a result, to generate enough power and voltage, many cells must be connected in series. Cell stacking is a technique for joining cells in a line.

Anode

A key part of solid oxide fuel cell, the anode is covered with an even layer of fuel. When hydrogen fuel oxidized at the anode terminal, electrons are released. These electrons travelled externally before reaching the cathode terminal. Strong electronic and ionic conductors that are also compatible with fuel cell components should be used for anodes. By fusing them with the proper electrolyte components, composite anode materials are created. Cobalt, copper, and nickel oxide are frequently employed in anode materials as catalysts, along with YSZ, GDC, and SDC electrolytes, and this may help us increase the performance of anode materials. The following are a few of the most important anode-related difficulties.

1. The porosity of the material could range between 20 and 40%.

2. Under high temperatures, thermal, chemical, and physical compatibility

3. Electrical and ionic conductivities have been improved.

4. A low resistance to polarization

5. A large triple phase boundary is present (TPB)

6. Particle size is fine and consistent.

7. Materials with a low cost

8. The thermal coefficient should match the components of fuel cell

Cathode

The cathode is fuel cell's positive end. The cathode's components have a perovskite-like structure. There are several common cathode materials: lanthanum strontium cobalt (LSC), lanthanum strontium magnetite (LSM), barium strontium cobalt iron oxide (BSCF), and lanthanum strontium cobalt iron oxide (LSCF) (LSCF). The following are some characteristics of good cathode materials.

1. Increased porosity of up to 30%-40% for diffusion.

2. Enhance ORR.

3. Decrease ASR.

4. Mechanical, chemical, and thermal compatibility with fuel cell part materials in real-world conditions.

5. Chemical reaction with a broad triple phase boundary.

6. Rapid chemical reaction to reduce oxygen levels.

7. Low cost and simple to synthesize.

8. Reduced polarization resistance.

9. The fuel cell components' thermal expansion coefficients must match.

Electrolyte

The electrolyte is a fuel cell's most important factor. The conductivity of electrolyte materials is used to measure a fuel cell's efficiency. The electrolyte used affects the operating temperature of the fuel cell since conductivity rises with temperature. Solid oxide fuel cells are more established

at high temperatures because of the solid electrolyte. In the section that follows, qualities of the best electrolyte are explained.

1. Exceptionally low electronic conductivity.

2. Increased density to keep the fuel from leaking.

3. High stability with both anode and cathode.

4. Ionic conductivity is increased. Additional ohmic losses result from low conductivity.

5. Increased density to keep the fuel from leaking.

6. Fuel cell materials should be mechanically, chemically, and thermally stable under working conditions.

7. Electrolyte materials should be inexpensive, adhesive, and simple to process.

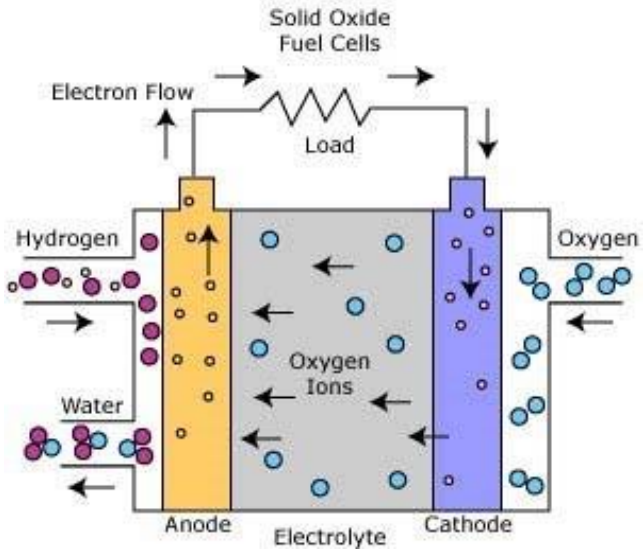

Figure 1.3: Schematic diagram of SOFC [34]

1.4.2 SOFC technology features

All solid-state construction and high-temperature functioning are the SOFC's key characteristics. This type of fuel cell has several distinct qualities and benefits because of the combination of these traits, including versatility in terms of stack and cell arrangements, production methods and power plant capacities.

Table 1.2: Characteristics of single-cell arrangements [31]

Self-supporting

Cell configuration	Advantages	Disadvantages
Electrolyte-supported	Dense electrolyte provides relatively robust structural support. Less vulnerable to failure because of cathode reduction (LSM cathode) and anode reoxidation (Ni/YSZ anode)	Low electrolyte conductivity results in higher resistance. An increase in operating temperature is necessary to reduce electrolyte ohmic losses.
Anode-supported	Anode with high conductivity Thin electrolytes are used to reduce operating temperature.	Anode reoxidation potential Thick anodes prevent mass transfer.
Cathode-supported	No oxidation problems, although there could be cathode reduction Utilize a thin electrolyte to reduce the operating temperature	Decreased conductivity Thick cathodes limit mass transportation

External supporting

Cell configuration	Advantages	Disadvantages
Interconnect-supported	Low-temperature components have thinner walls. Metal interconnections make for more robust building designs.	Connector oxidation The requirement for cell support limits the possibilities for flow field design.

Porous substrate	Low-temperature components have thinner walls. The potential for non-cellular material to serve as a support structure, hence enhancing attributes	Extra work required because of new components Problems with electrical conductivity could arise from the porous metal's uneven surface.

1.5 Fuel used in the cell

Fuel flexibility is the key benefit of SOFC. Of all fuel cell types, SOFC's cell is probably the most fuel-flexible because it can operate on a wide range of hydrocarbon fuels, including hydrogen, natural gas, ethanol, methanol and others. The adaptability of the fuel is very important because it gets around issues with cost, safety, etc. For testing the anode, I can use hydrogen, ethanol, and methane as fuel. Methane is among the most considered elective fuels for SOFCs since it is enough and principal ingredient of both common and biogas. A fluid fuel with a high energy density that can be stored and transported efficiently, ethanol also has a significant potential for producing hydrogen at high efficiencies with no net carbon emissions [35].

1.6 Fuel Cell Applications

One of the finest ways to get energy in a clean and safe environment is through fuel cells. There are many applications for fuel cells, including in home and business settings. Examples include internal insulation, portable power, spacecraft, office equipment, test facilities, door-to-door service in distant places, and electric cars.

1.7 Greenhouse effect and global warming

The earth's temperature rises because of greenhouse effect, which is phenomena caused by gases like carbon dioxide, methane, nitrous oxide, aerosols and water vapor absorbing outgoing infrared or long wave radiations [36]. The primary cause of changes in the world's climate is global warming carried on by greenhouse gas emissions. These emissions are strongly correlated with the world's rising energy demands [37]. Fossil fuel combustion is used for industry, transportation, power generation, and domestic purposes, but with all of these, it is also the main source producing atmospheric CO_2 emission and carbon dioxide, which are the well-known source of the greenhouse

effect. Over 70% of global energy consumption depends on high consumption of fossil fuels, and it is expected to represent 80% of global energy consumption over the next several decades. [38, 39]. According to the International Energy Agency (IEA), the burning of fossil fuels in creation of electricity accounts for around a third of carbon dioxide emissions. Coal, natural gas and oil make up 81% of all fossil fuel energy [40]. CO_2 is thought to be the gas that contributes most to the greenhouse gas impact based on two factors. The first component is the greatest CO_2 emissions, which account for up to 75% of all worldwide human emissions. The second issue is the length of time that CO_2 spends in the atmosphere, as it has a 300-year lifetime plus a 25% lifetime that never ends because of the use of fossil fuels [41].

Coal-fired power plants provide 33% of CO_2 emissions among thermal power plants that use fossil fuels, which are the industrial sources of carbon dioxide. It is predicted that this number would increase to 43% in 2030. As a result, the global CO_2emission is rising by more than 3.3% year [42]. Coal has now overtaken other factors as the main cause of increase in global temperature, since burning coal releases carbon dioxide into the atmosphere, which can raise average global temperature by more than 0.3 °C above pre-industrial levels [39], As a result, from preindustrial levels to the present, the atmosphere's CO_2 concentration has increased from 280 ppm to 370 ppm [43]. To keep the increase in global temperature to 2°C, the Intergovernmental Panel on Climate Change (IPCC) advised reducing CO_2 emissions by 2050 [44].

1.8 Chemical looping combustion (CLC)

Lewis and Gilliland first suggested CLC in 1954 to encourage the use of fossil fuels by generating pure CO_2. Later, Ishida et al. considered using CLC for power generation. It is the most promising new method for capturing CO_2 at a low cost and without the need for energy to separate the carbon. Additionally, the IPCC named CLC as one of the most economical methods in their special report on CO_2 collection and storage [45, 46]. According to the design put forth by Lyngfelt et al. in 2001, the CLC system consists of two reactors, a fuel reactor and an air reactor, which are connected by fluidized bed and have oxygen carriers flowing between them as shown in fig. 1.4 [47]. This setup is used in many CLC plants that have output powers between 10 and 100 kW. A CLC plant with a higher capacity of 0.5MWth was designed recently by a group of Koreans. Due to its low cost, the CLC technology has gained popularity in recent years on a global scale,

especially in the USA, Europe, and Asian nations like Korea, China, and Japan due to the emphasis on reducing carbon emissions on a global scale [48-50].

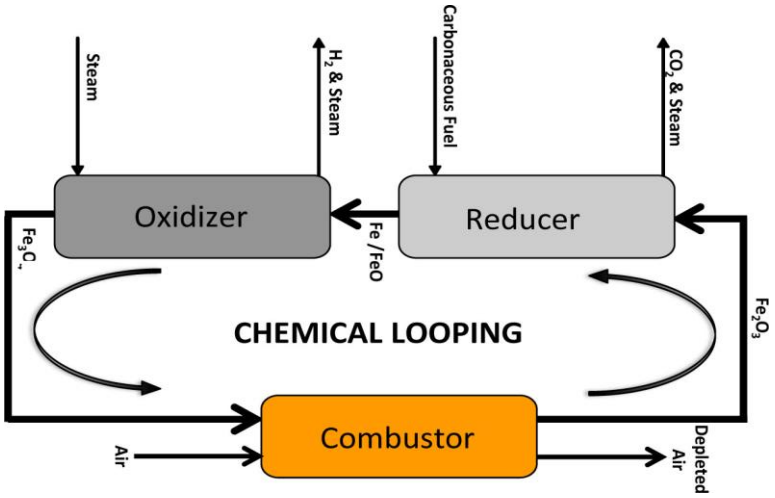

Figure 1.4 Simplified diagram of chemical looping reactor system [51].

1.8.1 Basic principles of CLC

Metal oxide is reduced in fuel reactors that either use biomass, natural gas, or coils, and the reduced metal oxide is then oxidized by gaseous oxygen in air reactors. The fuel is added to the fuel reactor and must be in a gaseous state. It must also contain metal oxide (oxygen carriers), which react with the fuel in the manner described below [52].

$$(2n+m)\ Me_xO_y + C_nH_{2m} \rightarrow (2n+m)\ Me_xO_{y-1} + nCO_2 + mH_2O \quad \textbf{(14)}$$

Only CO_2 and H_2O are present in the flue gas exhaust stream from a fuel reactor that has successfully converted all its fuel, from which pure CO_2 can be produced by condensing water and chilling the gas. The reduced and oxidized forms of oxygen carriers, respectively, are Me_xO_{y-1} and Me_xO_y. To prepare for the next cycle and prevent NO_x emissions, the reduced form of oxygen carrier is then transported to the air reactor for additional re-oxidation with air.

$$2Me_xO_{y-1} + O_2 \rightarrow 2Me_xO \quad \textbf{(15)}$$

Depending on the type of metal oxide (oxygen carrier) utilized and the oxygen carrier, the reduction reaction in CLC can be either endothermic or exothermic, but the oxidation reaction is

always exothermic. The two processes mentioned above (14) and (15), which involve direct contact between oxygen and fuel, release the same amount of energy overall [53].

1.9 Oxygen carriers Materials

The most crucial component in the process of CLC is oxygen carriers. They are known as oxygen carriers because they transmit oxygen from the air to fuel. For solid fuels, low-cost materials are examined, whereas for gaseous fuels, expensive and highly reactive materials are the main concern [54]. The usage of oxygen carriers' material produces thermal, mechanical, and chemical stress during oxidation-reduction reaction in the fluidized bed reactor system [55]. Within that repeated redox cycle, oxygen carriers must be reusable.

1.9.1 Characteristics of OCM

There are following some properties that must be attain by the oxygen carriers to be used in CLC technology:

- Oxygen carrier materials must be environmentally friendly i.e., have low risk for health and safety [56].
- They must be low in cost, minimum energy and production cost required for their manufacturing.
- They can transmit enough oxygen for the solid circulation ratio kept to minimum [55]. They must maintain their chemical, thermal and structural stability throughout a broad temperature range.
- Must be highly reactive to fuel, oxygen and able to totally convert fuel to CO_2 and H_2O.
- They should be resistant to attrition, fragmentation and have low inclination to clump together [57].

1.10 Oxygen Carriers used in literature

There are several oxygen carriers that have been utilized in literature but choosing the ideal one for the CLC process depending on several environmental factors, the lifetime of the materials, the fuel type used, and the operating conditions that will be used. Cu, Ni, Fe, Mn, and Co-based oxides account for the majority of the known effective oxygen carriers. The inert oxides, such as Al_2O_3,

SiO_2, ZrO_2, and $MgAl_2O_4$, combine with the metal oxides to strengthen them thermally and mechanically while also increasing their surface area for reaction by acting as a porous medium. These inert materials can also improve metal oxide's reactivity, porosity, and perhaps ionic conductivity while preserving its structural integrity [58].

1.10.1 Nickel based oxygen carriers

Because of their high reactivity towards methane, strength as a reforming catalyst, lack of ash, longer lifetime, and ability to show full fuel conversion when methane is used, nickel oxides were among the first materials identified and the most extensively studied for CLC process. With gaseous fuels, these metal oxides are used. Despite having all these advantages, nickel-based OCs are still unreliable for CLC because of their high-cost relative to other oxygen carriers and the fact that nickel ores do not contain an adequate amount of nickel. Because of its highly poisonous nature, NiO bring severe risk to the environment [59].

1.10.2 Copper based oxygen carriers

For the CLOU process, copper oxides are also used. CuO has high oxygen carrying capacity, quick reduction rate at all temperatures, and nearly complete conversion of methane into CO_2 and H_2O. Although these oxygen-carrying materials are substantially less expensive than NiO, they have drawbacks, including a low melting temperature that can cause agglomeration [60].

1.10.3 Cobalt based oxygen carriers

Despite having a high oxygen transport capacity and CLOU capability, cobalt oxide has received the least amount of attention in the literature. Due to their mechanical brittleness, incomplete conversion to H_2 and CO at high temperatures (800°C to 1200°C), high cost, and environmental concerns, these oxides are avoided [61].

1.10.4 Ilmenite based oxygen carriers

Ilmenite is the most affordable natural mineral employed as a prospective oxygen carrier material with solid fuels among all the least expensive minerals used for OC because of its extensive industrial uses. It can be found as $FeTiO_3$ ($FeO.TiO_2$), where iron oxide acts as oxygen carrier phase. When used as oxygen carrier, it is given $FeTiO_3$ in its reduced form. Due to its strong

attrition resistance, 100% theoretical combustion efficiency, and acceptable thermodynamic features, it is regarded as the finest oxygen carrier for CLC [62].

1.11 Iron Manganese based oxygen carriers

Iron-based oxides come in a variety of forms, including reduced forms like wustite (FeO) and simple Fe, oxidized forms like hematite (Fe_2O_3), and reduced forms like magnetite (Fe_3O_4). CLC reactions using iron oxide. The endothermic reaction with methane gas in the fuel reactor is shown in equation (16), and its byproducts, water, and carbon dioxide, are then further re-oxidized by air in air reactor (exothermic), as illustrated in (17) equation [63].

$$CH_4 + 12Fe_2O_3 \rightarrow CO_2 + 2H_2O + 8Fe_3O_4 \text{ (endothermic)} \quad \textbf{(16)}$$

$$8Fe_3O_4 + 2O_2 \rightarrow 12Fe_2O_3 \text{ (exothermic)} \quad \textbf{(17)}$$

Manganese oxides do not exist in metallic form, like other OCs. Under high temperature and pressure, these carriers show promise as CLOU materials. High attrition rates and incomplete oxidation when these carriers are created by impregnation prevent MnO from being widely regarded as an oxygen carrier despite its high reactivity, low cost, lack of agglomeration, and high oxygen carrying capacity [64].

1.12 Objectives

The major objective of this project is to develop and study the multifunctional metal oxides as an oxygen carrier for chemical looping and as cathode in fuel cells. Details of this project can be discussed in following steps,

- Literature survey by relevant journals that are highly related.
- Synthesis and preparation of metal oxides as an oxygen carrier using sol-gel method and solid-state reaction.

- The prepared materials will be analyzed both for chemical looping and fuel cells.

A variety of tools, including the ones listed below, will be used to characterize the materials in the processed samples.

i. X-ray Diffraction (structural studies)
ii. Scanning electron microscopy (morphology)
iii. UV-Visible spectroscopy (band gap)
iv. TGA thermogravimetric analysis (thermal stability)
v. Electrochemical impedance spectroscopy (EIS)
vi. Fourier transform infrared spectroscopy FTIR (bands)
vii. Oxygen transport capacity for CLC using TGA.

Chapter # 2

Literature Review

Ranjani Siriwardane et al. (2009) CLC can be utilized to produce partially deoxidized coal. When heated in either nitrogen or carbon dioxide (CO2), CuO demonstrated the best reaction properties of the coal/metal oxide mixture, starting the reduction reaction at temperatures as low as 500 °C and completing the full combustion at 700 °C. Carbon dioxide (CO_2) and water were found as the combustion products during the CLC reaction. X-ray diffraction and thermodynamic research demonstrated that the use of metal oxides as oxygen carriers in the development of CLC with coal is possible [65].

Anirban Nandy et al. (2016) CLC technology is being proposed as a viable option to reduce CO_2 emissions around the world. Oxygen is transferred from the air to the fuel via a metal oxygen carrier, which also sequesters carbon dioxide (CO_2) in the process. CLC processes have progressed thanks to the use of gaseous, solid, and liquid fuels; the creation of oxygen carriers; and the use of reactor systems. Pilot plant testing over the past few months has provided the necessary assurance to push this technique further in its development and toward commercialization. More study is needed to fully realize CLC technology's potential [66].

Zhuo Cheng et al. (2018) Clean and efficient hydrocarbon conversion via cyclic redox processes like CLC and CLR represent state-of-the-art technology. Metal oxide materials are necessary for the reduction of oxygen ions, and structural design and modification can increase their reactivity. Iron-based oxygen carriers are particularly appealing due to their high oxygen-carrying capacity, economic advantages, and versatility; however, there have been recent significant breakthroughs in oxygen carrier materials for several chemical looping applications. These developments will make it easier to create oxygen board materials for more effective industrial applications [67].

Doki Yamaguchi et al. (2021) improve the efficiency of chemical looping combustion. In a closed chemical looping reactor, they employed Australian ilmenite as an oxygen carrier and Victorian brown coal as fuel. The process requires 36 hours at 940-980 degrees Celsius at atmospheric pressure. The performance of CLC enhances with increasing the operating time and separated CO_2 concentration also increases from 2.3 to 8.9 over that time. Iron separation from bulk and its migration towards particle surface was also seen through results. Pores creation confirms the Hematite presence that was used to increase the OC reactivity and CLC performance [68].

Nhut M et al. (2021) using ilmenite and iron ore as oxygen carriers, the performance of syngas production from torrefied woodchips in a CLG is studied. The procedure was carried out in a bubbling fluidized bed reactor at the pilot scale. Ilmenite shows good reactivity at higher operating conditions like steam to biomass ratio and temperature. Steam addition in the CLG improves the hydrogen production and ilmenite also shows valuable performance towards hydrogen generation [69].

Ali Hedayati et al. (2022) studied the ilmenite and industrial iron ore as an oxygen carrier for chemical-looping combustion at 850℃ and 900 ℃ in a 0.3kw chemical looping reactor. The fuel used is synthetic biomass. Ilmenite show higher gas conversion, methane conversion, syngas to hydrocarbon ratio, and syngas fraction than the LD slag iron ore. These conversions of gases are higher for higher temperatures. They conclude that ilmenite has better gas conversion with suitable mechanical properties and is environment-friendly for the use of CLC and CLG [70].

Laingyong et al. (2022) investigated the change in micro-structure and variation in reactivity performance of ilmenite oxygen carrier under the varying temperature, chemical, and ageing effect. Changes in crystallinity, morphology, and the distribution of iron ions were shown to be the primary causes of microstructural modification in ilmenite. The oxidation of a redox reaction causes the iron element to migrate due to changes in temperature and oxygen concentration. Increased iron element concentration on the ilmenite surface and increased reactivity are both benefits of the lowering phase interaction between Fe_2TiO_5 and TiO_2 [71].

Zhihao Zhou et al. (2022) introducing a reducing ilmenite ore form as a catalyst for methane pre-activation will increase the reactivity of ilmenite towards methane gas. These 19 reduced ilmenite ore catalysts is useful for the CLG which uses ilmenite as oxygen carrier for syngas generation. Lower reactivity between ilmenite and CH_4 may hinder the process, so the addition of a catalyst that contains increased oxygen carrier ratio and temperature with a high reduction step was highly useful for promoting the reaction of CH_4 towards methane [72].

Chapter # 3

Experimental Procedure

3.1 Synthesis Techniques

The methods used to synthesize samples are Solid State Reaction (SSR), Vapor Phase Transport (VPT), Co-precipitation, Sol-Gel, Sputtering, Electrochemical, Hydrothermal, Flux growth.

3.2 Solid state method

Numerous compounds, such as mixed metal oxides, nitrides, and sulphides, can be produced using the solid-state approach. This process involves preparing two non-volatile substances for heating, where they react to produce the desired product. This procedure can also be used to prepare an extremely large number of chemicals. To accelerate the reaction using the solid-state approach, a high temperature, ranging from 500°C to 2000°C, was required.

- A homogeneous mixture of reactants was achieved by grinding.
- With intermediate grinding there were also a reaction time which was sometimes hours but may range into several days.
- Resistance heating were used by using furnace for heating the elements.
- Containers (crucibles) were used in furnace for reactions must be sufficiently inert to reactants and able to withstand high temperatures.

3.3 Preparation of Iron Manganese Oxide $Fe_xMn_{1-x}O$ (x=0.1, 0.2, 0.3)

Although the oxygen carrier material is also prepared using freeze-granulation and spray-drying techniques, in this project we used the solid-state method to produce such particles.

3.3.1 Materials

The following materials which are in nitrate form are used as starting materials for the synthesis of Iron Manganese.

Table 3.1: Material's composition

Chemical name	Molecular formula	Molecular weight
Iron (III) nitrate	$Fe(NO_3)_3$	404.06 g/mole
Manganese nitrate	$Mn(NO_3)_2$	251.01 g/mole

3.3.2 Apparatus

The following apparatus was used for the sample preparation:

- Weight balance to measure the materials.
- Aluminum foil
- Spatula
- Agate mortar and pestle for grinding
- Crucibles
- Furnace
- Sample tubes

3.3.3 Calculations

$Fe_xMn_{1-x}O_3$ (x=0.1, 0.2, 0.3) chemicals were synthesized by solid-state reaction. From formula 0.1, 0.2, 0.3 grams for iron and 0.9, 0.8 0.7 grams of manganese were taken respectively, but only 10g of total sample is used to avoid wasting materials.

3.3.4 Methodology

5.739 g of Iron nitrate Fe $(NO_3)_3$, 14.26 g of Manganese nitrate Mn $(NO_3)_2$ with weight balance for first sample. All these chemicals were homogenized by grinding using agate mortar and pestle. This powder poured into the crucible. Then the crucible filled with the material were placed in drying oven first for 3hrs and then in digital muffle furnace and sintered at 300℃ for half hour with stepwise increasing temperature. Then the last step was the grinding of sintered material again in the agate mortar and pestle for obtaining the soft homogeneous powder. After the fine powder is obtained, put into the sample bottles for further characterizations. Samples second and third prepared in the same way but with different concentrations of iron manganese about 3.146g and 6.853g used for sample II and 4.404g and 5.595g used for sample III respectively.

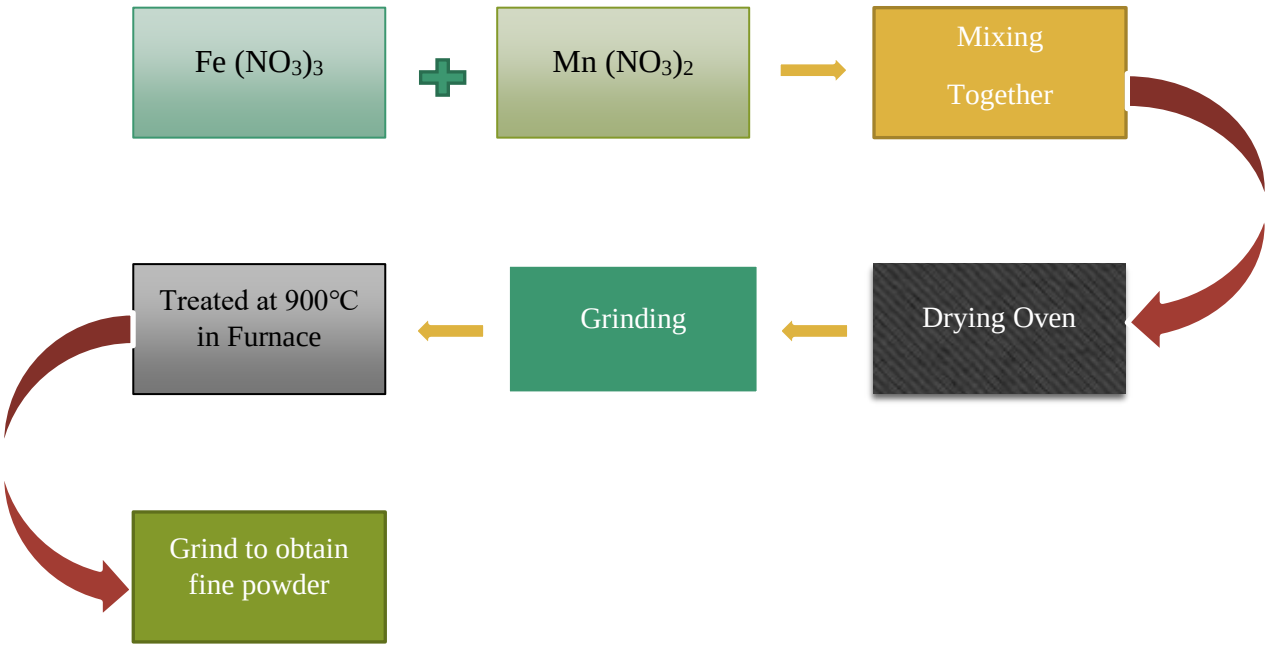

Flow Chart of synthesis of synthesized material $Fe_xMn_{1-x}O_3$ (x=0.1, 0.2, 0.3).

3.4 Preparation of Samarium doped Ceria (SDC)

The material's precursors were cerium nitrates hexahydrate, samarium nitrate hexahydrate, and sodium carbonate (Na_2CO_3). The nitrates and precipitate agent were mixed in a 1:1 molar ratio, Separately, both chemicals were mixed in deionized water. These solutions were then sundried and stirred for 60 minutes. This mixed solution was heated to 80°C to achieve a homogeneous solution. The Na_2CO_3 solution was prepared by mixing it with DI-water for 80 minutes at 80°C. The precipitate agent was added dropwise to the samarium and cerium solution. The mixture was then constantly stirred at 500 rpm for two hours at 80°C. Then left it alone overnight in titled shape. The precipitates that formed were filtered using vacuum pump filtration and washed three times with DI water. These were then dehydrated in drying oven at 100°C for 4 hours. The dried powder was then sintered in the crucible for 4 hours at 500°C. The nitrates were evaporated at temperatures between 250°C and 300°C. The mortar and pestle were used to grind the resulting product into a fine powder.

3.5 Composite Materials

For the synthesis of composite materials, a few techniques are used, including the sol-gel method, co-precipitation method, hydrothermal method, freeze granulation method, and solid-state reaction

method. Solid state reaction method was used in this research study to mix components and create composite materials since it is more effective, less expensive, and simpler than other methods.

3.5.1 Materials

The following materials which are in nitrate form are used as starting materials for the synthesis of Iron Manganese with SDC based oxygen carrier.

Table 3.2: Material's composition

Chemical name	**Molecular formula**	**Molecular weight**
Iron (III) nitrate	$Fe\ (NO_3)_3$	404.06 g/mole
Manganese nitrate	$Mn\ (NO_3)_2$	251.01 g/mole
Samarium (III) nitrate hexahydrate	$Sm\ (NO_3)_3 \cdot 6H_2O$	4.075 g/mole
Cerium (III) nitrate hexahydrate	$Ce\ (NO_3)_3 \cdot 6H_2O$	15.92 g/mole

3.5.2 Calculations

$Fe_xMn_{1-x}O_3$ (x=0.1, 0.2, 0.3) with SDC_x (x=10%, 20%) chemicals were synthesized by the solid-state reaction. From formula 1.8, 1.6 grams for iron manganese with 0.2, 0.4 grams of samarium doped ceria were taken respectively, but only 2g of total sample is used to avoid wasting materials.

3.5.3 Methodology

$Fe_xMn_{1-x}O_3$ (x=0.1, 0.2, 0.3) mix with SDC_x (x=10%, 20%) by grinding using agate mortar and pestle. The powder poured into the crucible. The material was sintered in a digital muffle furnace at 1050°C for 5 hours, with the temperature gradually rising throughout the process. The final process involved grinding the sintered substance once more with the agate mortar and pestle to produce a fine, uniform powder. The obtained fine powder was then transferred to the collection bottles for analysis. Samples second and third prepared the same way but with different concentrations of iron manganese with SDC.

3.6 Cell fabrication

After the preparation of the materials, the powders were taken in an appropriate quantity and compressed into pellets using a Carver hydraulic press, as seen in figure 3.1. The pressing process used dry powder. It requires filling stainless-steel dye with the powders and pressing it in a single motion at an applied load of 3000 Mpa to create an entire cell.

Figure 3.1: Hydraulic press

Figure 3.2: Cell (pellet) without silver paste

Figure 3.3: Cell (pellet) with silver paste

According to Figure 3.2, each cell had a diameter of 9 mm and an active area of 0.64 cm^2. To create dense pellets, these cells were sintered at 650^oC for 20 minutes. Figure 3.3 demonstrates

how the current collection's cells were coated with silver paste on both sides. Utilizing the manufactured pellets, conductivity is measured. A complete cell is created for fuel cell performance, including the electrolyte in the middle and the cathode and anode on either side.

3.7 X-Ray Diffraction

In the fields of solid-state chemistry and materials research, X-ray diffraction (XRD) is a crucial characterization technique since it provides the most precise structural data (including interatomic distances, bond angles, crystallinity, and others). The extensive use of X-rays for investigation of atomic structural arrangements is since their wavelength is in the 1 x 10^{-10}m region, which is the same order of magnitude as atomic spacings in crystalline materials. When x-rays interact with a crystal lattice, a simple model known as Bragg's rule can be used to comprehend the needs for diffraction. The Bragg's law can be stated as follows:

$n\lambda = 2d\sin\theta$

where λ is the wavelength of X-ray, d is the spacing between layers of atom, θ is angle between incident X-ray beam and scattering plane, and n is integer.

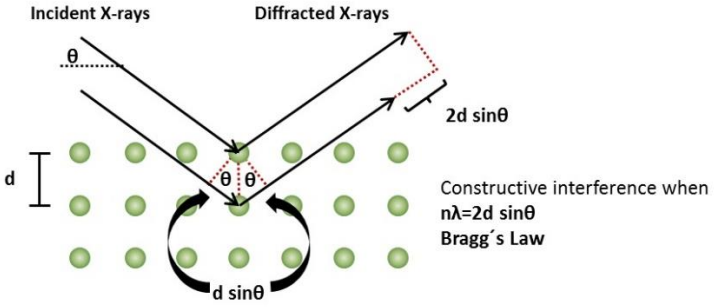

Figure 3.4 X-Ray diffraction pattern [73]

As a result, if atoms are arranged in periodic form crystals, the diffracted waves will consist of sharp interference maxima (peaks) with the same symmetry as in the distribution of atoms. It is also possible to learn about the crystals' internal structure by observing the diffraction peaks [74, 75].

3.8 Raman Spectroscopy

Raman spectroscopy is a non-destructive method of chemical examination that provides detailed information about crystallinity, chemical structure, phase and polymorphy and molecular interactions. It is based on the interaction of light with the chemical bonds of a substance.

By scattering off a molecule with a powerful laser, the Raman method is a sort of light scattering. Rayleigh scattering occurs when most of the scattered light has the same wavelength (or color) as the laser source, delivering little meaningful information. Raman Scatter occurs when an analyte's chemical composition leads it to scatter light at various wavelengths (or colors).

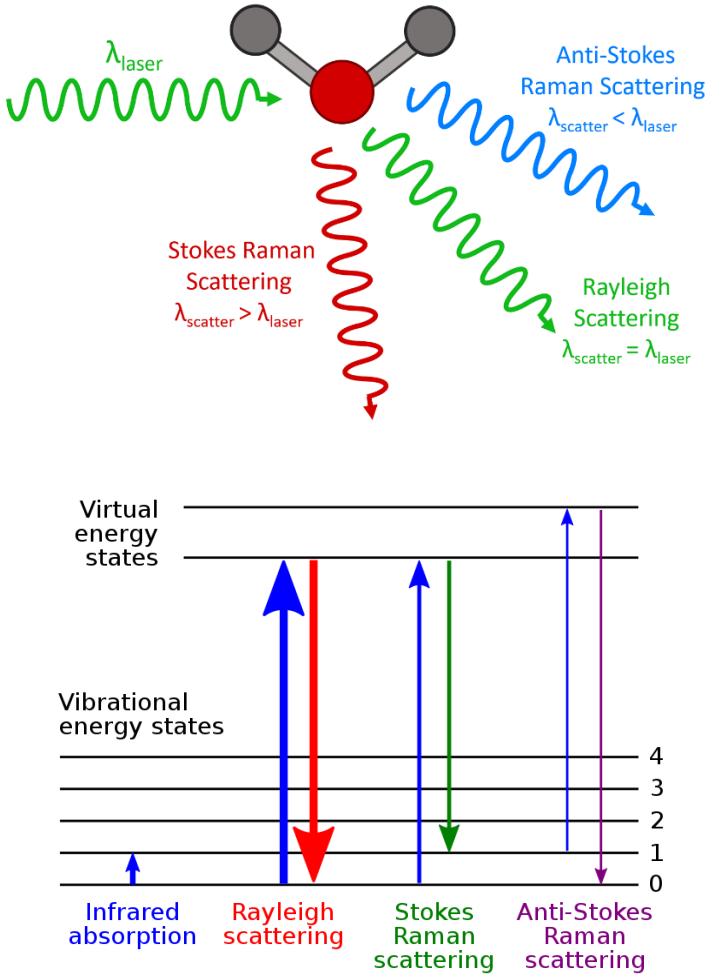

Figure 3.5 Raman Spectra's energy level diagram depicting the states

Multiple peaks in a Raman spectrum indicate the relative intensity and wavelength of Raman scattered light. Different types of chemical bond vibrations are represented by different peaks, for

example, the breathing mode of the benzene ring, polymer chain vibrations, and lattice modes. Some examples of single bonds are C-C, C=C, N-O, and C-H [76].

3.8.1 Information provided by Raman spectroscopy

Raman spectroscopy examines a material's chemical composition and provides details about:

- Chemical structure and identity
- Phase and polymorphism
- Intrinsic stress or strain
- Contamination and impurity

In many cases, a Raman spectrum can be used to swiftly identify the drug in question or to differentiate it from other chemicals with similar spectra. Raman spectral libraries are commonly used for material identification using Raman spectra. The analyte's spectrum is compared to a database of hundreds of spectra, and a match is promptly found.

Raman mapping (or imaging) systems can use the sample's Raman spectra to create images. Different crystallinity types, polymorphs, and phases can be seen in these images [77].

3.9 Fourier Transform Infrared Spectroscopy

The Fourier transform is the method used in infrared (IR) spectroscopy. In infrared spectroscopy, infrared light is used to illuminate the sample, with some of the light being absorbed and some being transmitted. The resulting spectrum from infrared spectroscopy displays molecule absorption and transmission, providing a molecular fingerprint of the material. The absorption peaks in the spectra are directly proportional to the molecular vibration frequencies. The material's concentration can be inferred from the magnitude of the peak in the spectrum [78].

The slow scanning technique was addressed by FTIR, which provides all IR frequencies simultaneously. When an FTIR sample interacts with an interference wave, the interacting energy is thought of as having a specific wavelength range. This form of signal, which is created by an interferometer, contains all the infrared frequencies. The wavelength of the sample's infrared absorption was measured. Consider to be at the x-axis in FTIR. The wavenumber at which the sample absorbs IR light is shown at the top of the peaks. Infrared absorption by functional groups

can cover a wide spectrum because of the intricate interactions between atoms within a molecule [79, 80].

It has been found, however, that many functional groups, regardless of their interactions with the rest of the molecule, generate unique IR absorption at certain, limited frequency ranges. The sample's absorption spectra are determined using following equation,

$A=\log (I_o/I)$

Where A is the absorbance, I_o is the radiant power incident on the sample, I is the radiant power transmitted by the sample. Range of absorbance is from infinity to zero. Absorption for a single compound in a homogeneous medium is presented as

$A=abc$

A =measured sample absorbance at the given frequency

a = is the molecular absorptivity at the frequency,

b = is the path length of the source beam in the sample

c= is the concentration of the sample.

In a homogeneous medium, the strength of the absorption band is proportional to the concentration of the individual components, as described by the Bouguer Beer Lambert law [81].

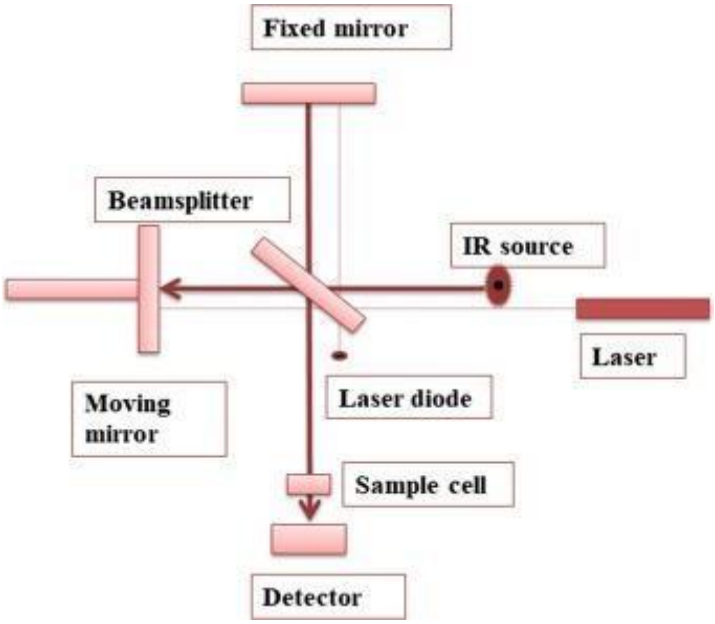

Figure 3.6 : Operation of FTIR [82]

In figure 3.6, a beam splitter divides an infrared (IR) light beam into two parts, with one half passing through a fixed mirror and the other half passing through a mirror that moves with a constant speed. An interference pattern is produced by reflecting and recombining the recombination's destructive and constructive interference. The sample is then given this interference pattern, and the transmitted portion of the interference pattern transferred to a detector. The entire spectrum is collected as a function of wavenumber after being compared to a reference sample beam spectra in the detector [83].

3.10 Thermogravimetric Analysis (TGA)

This experimental approach considers the mass of the sample as a function of either time or temperature. For sample measurement, a consistent environment and temperature are utilized. Due to the atmosphere's important significance as a reactive, oxidizing, or inert substance in the TGA experiment, it is also taken into consideration. Measurements may also consider changes in the atmosphere. A TGA curve illustrates the mass measurement obtained from TGA analysis by plotting mass or percent versus either time or temperature [82].

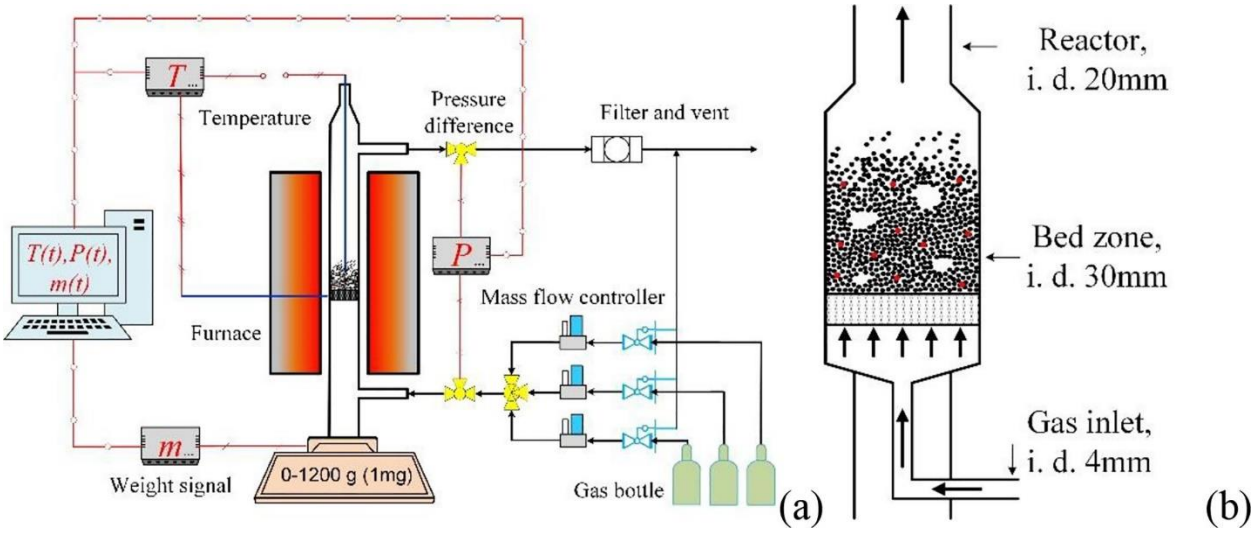

Figure 3.7 (a) The MFB-TGA, in schematic form and (b) fluidized bed reactor particle weight distribution diagram [84]

After loading the reactor with material, hot argon is used as the fluidizing agent. Once the temperature has stabilized, rapid heating can be achieved by applying a gas flow via a fluidized bed. To simulate the process, nitrogen is used during the balance [85].

Thermogravimetric analysis (TGA) is one of numerous experimental techniques used to determine an oxygen carrier's precise and steady temporal mass change to quantify its redox kinetics. Redox reactions started under inert conditions with N_2 toward the reaction gas when particle heating and mixing were carried out in the TGA at room temperature. Between oxidation and reduction cycles, inert gas was supplied to prevent the mixing of H_2 and O_2 [73].

The mass-based reduction rate or fractional conversion of reduction can be calculated as

$$xr = \frac{mo-m}{mo-mr} = \frac{mo-m}{Romo} \qquad \textbf{(18)}$$

where m is the instantaneous weight of the oxygen carriers, mo is the initial weight before reduction, and mr is the final weight after reduction. Similarly for oxidation fraction we can use the following equation.

$$xo = \frac{m-mr}{mo-mr} = \frac{m-mr}{Romo} \qquad \textbf{(19)}$$

Ro is the oxygen transport capacity; we can say that during the oxygen transfer mass fraction of the OC was used. [85]

$$Ro = (\frac{mo-mr}{mo}) \times 100 \quad \textbf{(20)}$$

3.11 Conductivity Measurement

The ability of a metal or a gas—in other words, all materials—to pass an electric flux is known as conductivity. Cations and anions carry the current in solutions, whereas electrons carry it in metals. The solution's ability to conduct electricity depends on a variety of factors.

• Concentration

• Mobility of particles

• Valence of particles

• Temperature

It's important to include both electron and proton conduction when estimating a material's conductivity. Conductivity is measured in S/cm^2. The DC conductivity of the sample pellets is measured using two contact methods.

- Electrochemical Impedance Spectroscopy (EIS)
- 4-point probe method

3.11.1 Electrochemical Impedance Spectroscopy (EIS)

Electrochemical impedance spectroscopy is used to measure how an electrochemical system reacts to a functional voltage. This is totally reliant on how frequently it is used. Physical and chemical events can be far distant and well-known at a particular applied potential using just one experimental technique for EIS, which can span a wide enough range of frequencies. In figure 3.8 EIS measurements setup.

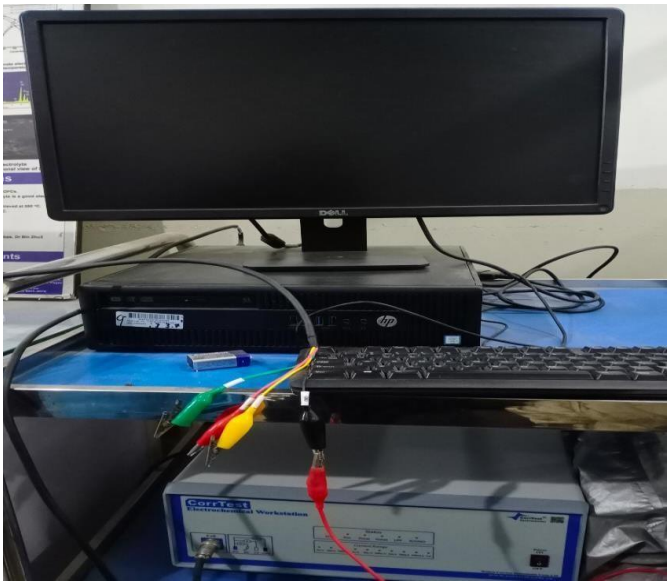

Figure 3.8 EIS measurement setup

A small amplitude sinusoidal excitation signal is applied to the system under examination to start off every impedance measurement, and the response is then measured. Ohm's law can be used to compute the system impedance.

$$Z(\omega) = E(\omega) / i(\omega)$$

The impedance Z is a complex ratio whose amplitude and phase shift are determined by the frequency of the signal. The impedance is therefore a function of frequency when the signal's frequency is changed. The Nyquist Plot is a graph that contrasts the real and imaginary components of impedance. The Nyquist representation has the benefit of offering a summary of the data and enabling qualitative evaluations. When charting data in a Nyquist presentation, the real axis must match the imaginary axis exactly to prevent distortion of the curve's shape. Gaining a qualitative understanding of the data requires understanding the curve figure [73].

3.11.2. 4-point probe method

The four-probe DC method is in fact the most effective for anode materials. Measurements of conductivity were made using the DC conductivity shown in figure 3.9. The four-probe approach yields the most accurate results for measuring DC conductivity since it makes use of four terminals.

Figure 3.9 KD2531E low resistance ohmmeter for DC conductivity measurements

3.13 Fuel Cell Testing

Two terminals in u-shaped are used in the fuel cell testing technique. Two connections in the device's center were utilized to transfer air to the cathode after the prepared cell had been attached there. The cathode side is where the fuel is applied. The dye was put in the furnace to heat it up to the desired temperature so that we could measure the performance. Values of the voltage and current were measured once the temperature reached the limit. Next, create the current density and power density curves based on the reading. Below is a figure for testing fuel cells.

To create a fuel cell, three layers of electrode were produced.

- We can take 0.3g of pre-made samarium doped ceria (SDC) electrolyte material from the lab and 0.4g of anode material. The lab allows us to remove 0.3g of (LNCZ) cathode material in a similar manner.
- Then, using a hydraulic press and sintering for an hour at 700°C, we may create a pallet of 1g.
- After that, the cell was heated in the furnace, and its activation temperature was measured.
- For testing the cell, we can utilize three different fuels: hydrogen, natural gas, and ethanol.
- The temperature was then properly ordered extended, execution was assessed by computing the Open Circuit Voltage (OCV), and then a load was applied to gradually grow the load and calculate the current.
- The formula $I_d = I/A$, where A is active area of the pallet and I is current, will then be used to compute the current density.

- Like this, the three cells' performance is attained by utilizing various fuels.

Chapter # 4

Results and Discussion

The results obtained by various characterization techniques, including FTIR spectroscopy, Raman spectroscopy, UV-Vis spectroscopy, will be discussed in this section. These strategies were used to investigate various facts of materials, including analysis of structures, molecular vibration, bonding present in the material, energy band gap, conductivity, and outcomes.

4.1 FTIR spectroscopy Analysis

The following 4.1, 4.2, and 4.3 figures displays the FTIR spectra that were produced by the material $Fe_xMn_{1-x}O$-SDC_x (x=10 wt.%, 20 wt.%) using the solid-state reaction technique. Because iron manganese metal oxides are a porous material, diagrams displaying $Fe_xMn_{1-x}O$ show transmittance. However, when we combine SDC with iron manganese, the porosity of the material decreases, and the material demonstrates absorbance. Peaks in the $Fe_xMn_{1-x}O$-SDC 10% concentration are higher than those in the $Fe_xMn_{1-x}O$ and $Fe_xMn_{1-x}O$-SDC 20% concentrations. It can be argued on behalf of obtained FTIR spectra that the 10% SDC concentration with $Fe_xMn_{1-x}O$ produces superior results. Since, $Fe_xMn_{1-x}O$ is a cathode substance that exhibits characteristics of an electronic nature, whereas SDC is an electrolyte that exhibits characteristics of an ionic nature. .The more ionic substance contents addition like 20%SDC or even more, the $Fe_xMn_{1-x}O$ cathode material may turn towards ionic state.

In the graph, there are slight peaks at 1633cm^{-1}, 1647cm^{-1}, 1650$cm^{-1}$and 1654cm^{-1} that show the bending vibrations of water molecules. In the region 1300 cm^{-1} to 1600cm^{-1} the O-C-O stretching band is observed. The absorption peak at 670cm^{-1} and 677cm^{-1} and 665cm^{-1} may show the stretching vibrations of Fe-O (Fe_2O_3, γFe_2O_3) presence peaks of iron and oxides exist below 800cm^{-1} or between 400cm^{-1} to 800cm^{-1} wavenumber [86-88]. Some weaker peaks at the region around 3600cm^{-1} to 3800cm^{-1} shows the stretching vibration of O- H. The O-H bending vibrations associated with Mn atoms are reflected in the 1046.9 cm^{-1} absorption bands [89]. C-H stretching vibrations were assigned to the peaks at 2931 and 2898 cm^{-1}, and C-H bending vibrations of the methylene (-CH2-) groups in the triethanolamine ligand were assigned to the bands between 1450 and 1200 cm^{-1}. O-H stretching and O-H bending overtones were ascribed to the bands at 3355 and 1634 cm^{-1}, respectively. These bands were most likely caused by the complex absorbing water. In specifically, the band at 1072 cm^{-1} resulted from the samarium doping's Sm-O-C vibration and/or the Ce-O-C stretching vibration. The band at 566 cm^{-1} was also found to have Ce-O and/or Sm-O peaks [90].

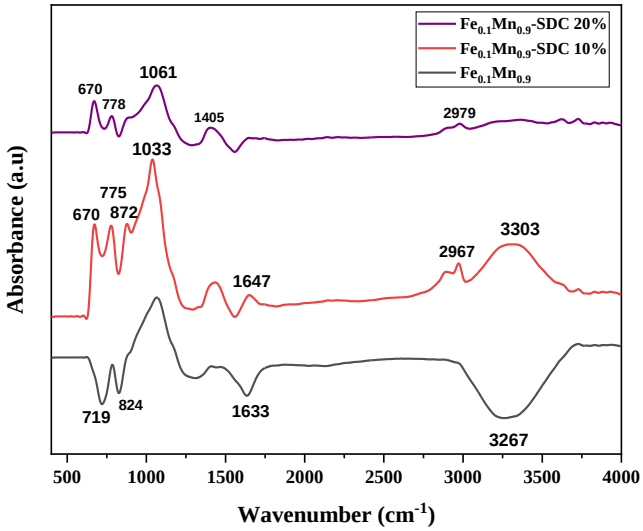

Figure 4.1 FTIR analysis of Fe0.1Mn0.9O-SDCx (x=10 wt.%, 20 wt.%)

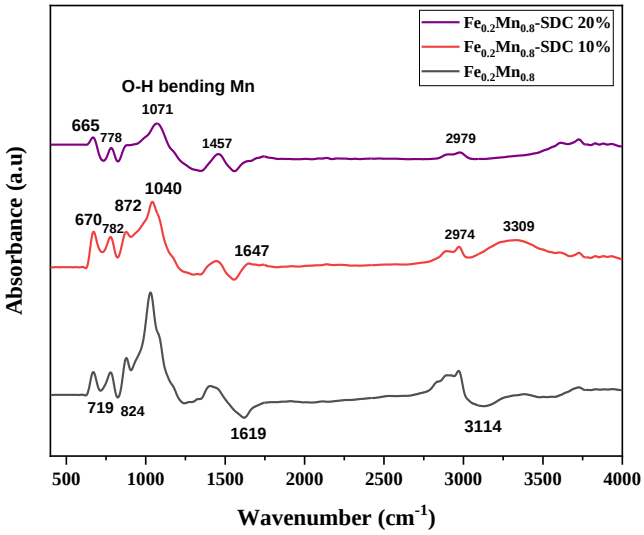

Figure 4.2 FTIR analysis of Fe0.2Mn0.8O-SDCx (x=10 wt.%, 20 wt.%)

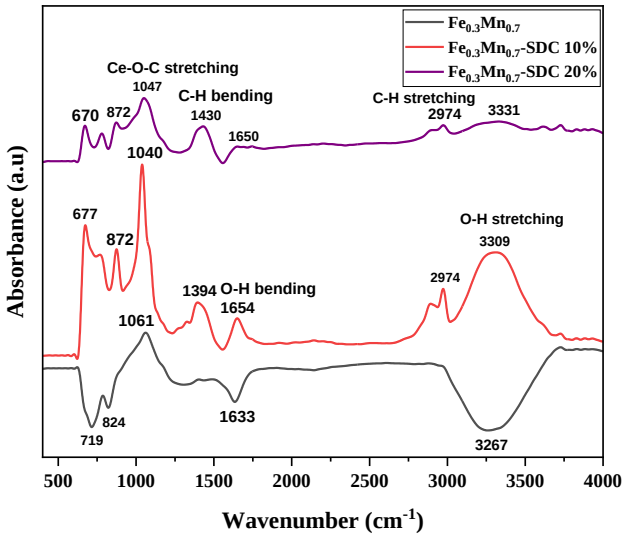

Figure 4.3 FTIR analysis of Fe0.3Mn0.7O-SDCx (x=10 wt.%, 20 wt.%)

4.2 Raman Spectroscopy Analysis

The Raman spectra of our synthesized materials $Fe_xMn_{1-x}O$-SDCx (x=10 wt.%, 20 wt.%) were obtained by RENISHAW in Via TM Qontor® confocal Raman microscopy using a laser of 514nm wavelength. In Raman spectroscopy structure, molecular fingerprints, and vibrational modes are revealed. Raman scattering, which employs inelastic light scattering, may be used to detect molecular vibrational spectroscopy. Raman spectroscopy uses the scattering of a laser photon by a sample molecule to determine whether it is losing or gaining energy. The energy amount lost was represented by a change in photon energy. This energy loss is a characteristic of each molecule's particular bond. A precise spectral mark that might be unique to a molecule or a single molecule structure is produced by Raman spectroscopy.

Figure 4.4, 4.5 and 4.6 represents Raman spectra of $Fe_xMn_{1-x}O$-SDC_x (x=10 wt.%, 20 wt.%) respectively. As shown in the figures different intensity peaks were observed in this Raman spectra. According to the literature the band of 669cm^{-1} and two small peaks of 340 and 527cm^{-1} corresponding to A_{1g}, T_{2g}, and E_g modes for Fe_3O_4, respectively [91]. The broad band at 669 cm^{-1} is usually associated with magnetite Fe_3O_4, but it has been detected in Fe_2O_3 compounds as well [92], where it has been hypothesized that it corresponds to the prohibited Raman mode LO Eu. The development of the LO Eu prohibited band has been hypothesized to result from a breakdown

in the symmetry governing the dispersion of LO-phonons [93, 94]. Some nanostructures' surfaces and solid solutions both exhibit structural disorder. The symmetry features of LO-phonon dispersion can be perturbed by the exact irregularity of the surface of 1D metal-oxide nanomaterial. Hematite's 611 cm^{-1} peak may have a second harmonic between 1320 and 1330 cm^{-1}.

Additional broad asymmetric bands may be seen in the sample's Raman spectrum at 530 and 1050cm^{-1}. In the manganosite MnO phase, the low frequency band at 530 cm-1 has been previously attributed to 2TO [95, 96] or LO phonons. The formation of the 1050cm^{-1} high-frequency band is complicated, as it encloses two bands with connections to the TO+LO (a band wing at 950 cm^{-1}) and 2LO modes [97] in the manganosite MnO phase. Weak intensity of the intermediate band from 2TO modes is hidden by a narrow band contribution at 660 cm^{-1} from the Mn_3O_4 phase.

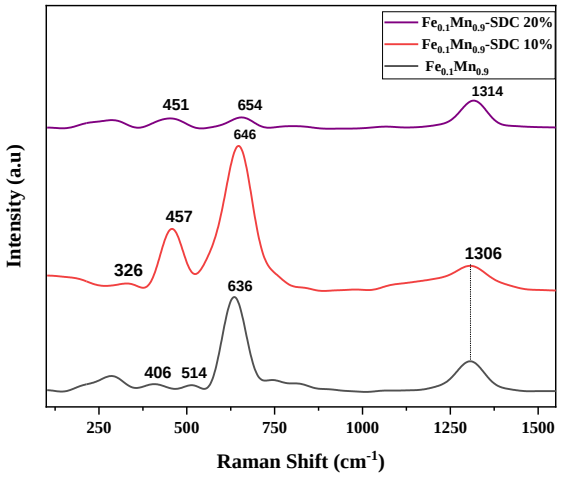

Figure 4.4 Raman spectra of Fe0.1Mn0.9O-SDCx (x=10 wt.%, 20 wt.%)

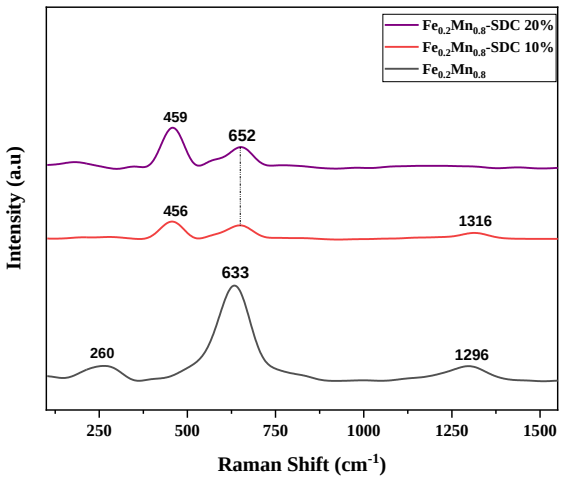

Figure 4.5 Raman spectra of Fe0.2Mn0.8O-SDCx (x=10 wt.%, 20 wt.%)

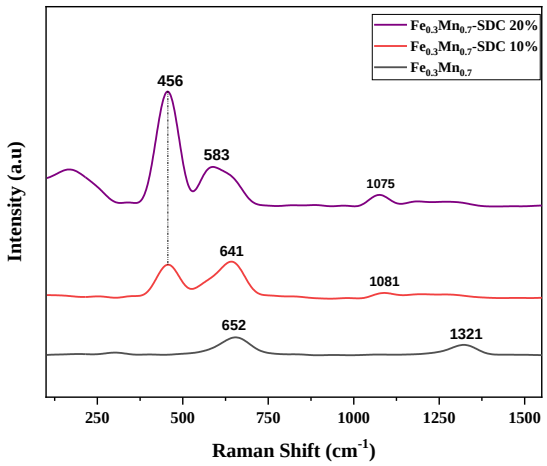

Figure 4.6 Raman spectra of Fe0.2Mn0.8O-SDCx (x=10 wt.%, 20 wt.%)

4.3 Scanning electron microscopy(SEM)

Scanning electron microscopy was used to characterize the morphology of the best oxygen carrier that had been synthesized with 10% and 20% samarium doped cerium. Up to a magnification of 12500x was used to complete the study. The photograph reveals the sample's granular structure with interstices between the grains. Iron manganese oxides become porous after being subjected to multiple reduction-oxidation cycles, which results in the formation of macropores or fissures. Figures (a), (b) and (c) shows SEM of $Fe_xMn_{1-x}O$ (x=0.1,0.2,0.3). Figures (d), (e) and (f) shows SEM of $Fe_xMn_{1-x}O$ (x=0.1,0.2,0.3)-SDC (x=10 wt.%). Figures (g), (h) and (i) shows SEM of

$Fe_xMn_{1-x}O$ (x=0.1,0.2,0.3)-SDC (x=20 wt.%). CeO_2 effects show spherical morphology of particles with very homogeneous and smoothed grain structure. Active-phase surface is confirmed by granular structure generation. These grains promoted the reaction surface area that's the reason for rising the reactivity of iron manganese with an increasing number of redox cycles [98].

The results showed that the shape and surface areas of the produced oxygen carriers were not significantly altered by the addition of CeO_2. Miller's observation that CeO_2 had no effect on the hematite surface area is supported by these results. [99].

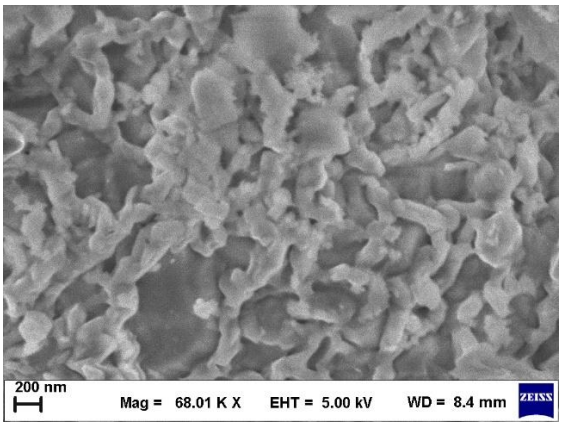

(a)

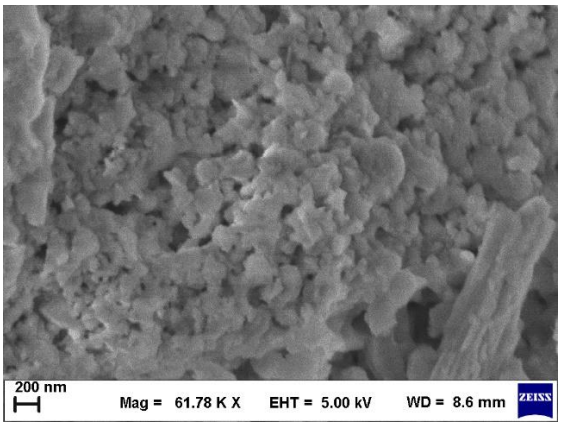

(b)

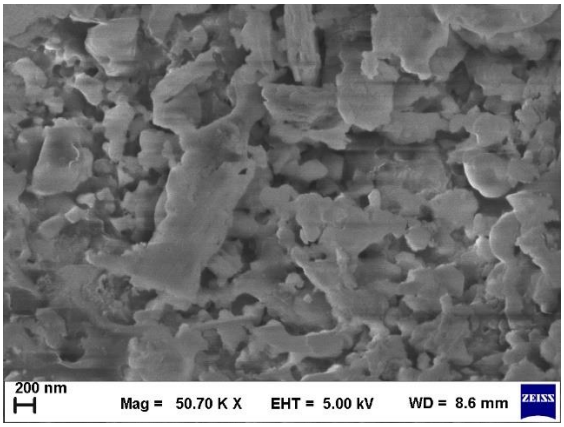

(c)

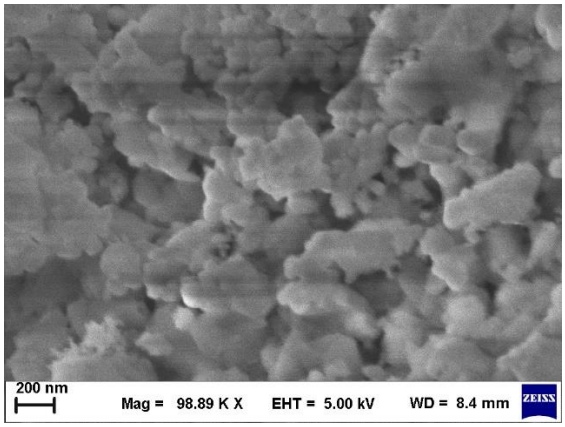

(d)

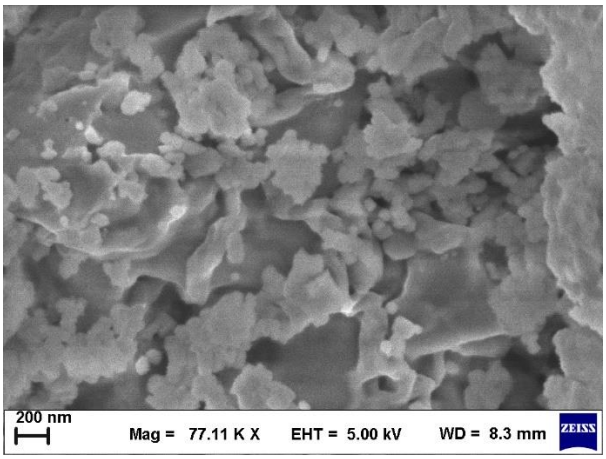
200 nm
Mag = 77.11 K X
EHT = 5.00 kV
WD = 8.3 mm
ZEISS

(e)

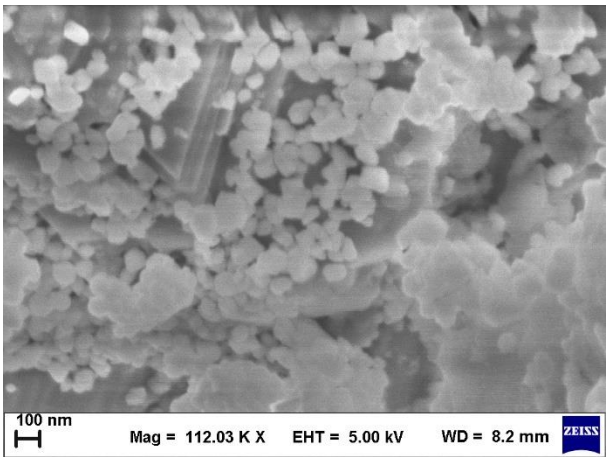
100 nm
Mag = 112.03 K X
EHT = 5.00 kV
WD = 8.2 mm
ZEISS

(f)

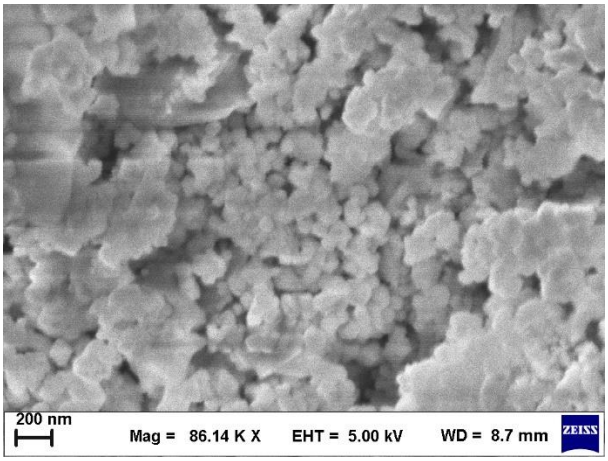
200 nm
Mag = 86.14 K X
EHT = 5.00 kV
WD = 8.7 mm
ZEISS

(g)

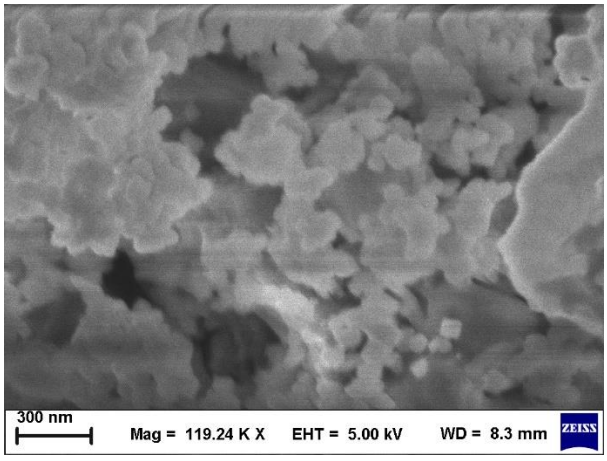
300 nm
Mag = 119.24 K X
EHT = 5.00 kV
WD = 8.3 mm
ZEISS

(h)

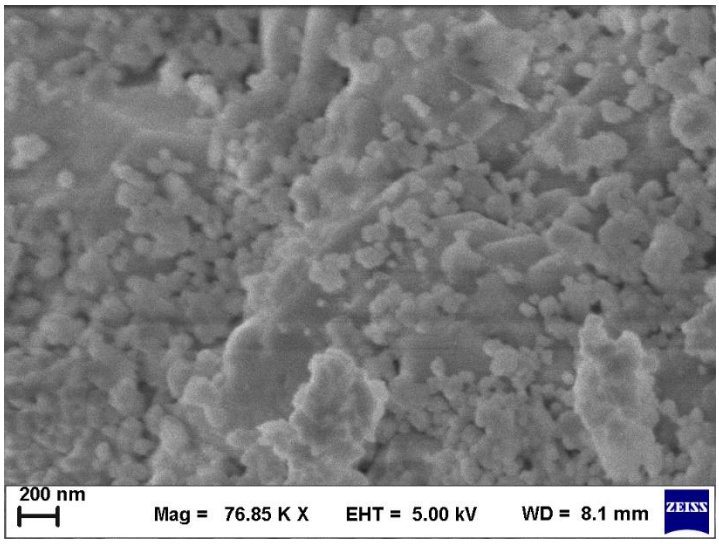

Figure 4.7 SEM image of sample

4.4 X-Ray Diffraction

Below a graph shows the X-ray diffraction spectra of our material $Fe_xMn_{1-x}O$-SDCx (x=10 wt.%, 20 wt.%) prepared by the Solid-State method. Structure properties were characterized using x-ray diffraction (XRD). The crystallite size and internal stresses affect the broadening of X-ray diffraction lines. Changes in the peak broadness and amplitude are caused by internal strain and charge imbalance, which in turn is caused by a higher ionic radius of Ce^{4+}, charge deficiency, and oxygen vacancy [100]. This indicates that the structure we obtain is poorly crystalline or in the micro-crystalline phase which shows the presence of micro strain.

Our pattern of the synthesized material shows the diffraction peaks indexed at 33.40º(222), 47.93º(331) and 56.40º(511) for $FeO.Mn_2O_3$ having face centered cubic phase and space group of $FeO.Mn_2O_3$ is Fd3m card no.00-002-1388 and for cerium oxide diffraction peaks indexed at 28.68º(111), 47.83º(220), 59.59º(222), 64.58º(400), 76.80(331), 79.07º(420), 88.89º(422) with cubic phase and space group Fm-3m card no.00-001-0800 for CeO_2 . lattice parameters of iron manganese oxide are a=b=c=8.4700Å and lattice parameters of cerium oxide are a=b=c=5.41Å. A small peak at the 25.5º shows the Brookite MnO_2 presence. The above result shows the spinal shape structure of iron oxides [101]. A peak at 18º(002) shows diffraction of iron oxide nanoparticle [102]. At 25.6º peak shown with indices (012) indicates the Fe_2O_3 through literature[103].

Average crystalline size of the particle is calculated by using well known scherrer formula

$D = k\lambda/\beta\cos\theta$

Value of crystallite size of the particle was calculated for high intense peak of cerium oxide with indices of (111).

Table 4.1: Characteristics of cerium oxides from XRD pattern

Sample	2θ	Lattice parameter Å	D(hkl)nm
1	29.12°	3.07	46.43
2	28.87 °	3.08	39.20
3	28.76 °	3.10	43.45

Lattice parameters and crystalline size has an inverse relation. When size decreases, lattice parameter increases. It is also due to the increase in surface to volume ratio by decreasing particle size which create high contribution of surface layer unpaired electrons. So, we conclude that lattice parameter is larger in small size than in bulk [104].

Table 4.2: Characteristics of XRD obtained phases

Phase	Characteristics	X= 10%	X= 20%
FeMnO	Crystalline size Crystal structure Space group	56.40 Cubic Fd3m	47.93 Cubic Fd3m
SDC	Crystalline size Crystal structure Space group	33.40 Cubic Fm-3m	88.89 Cubic Fm-3m

Table 4.2 shows some characteristics of iron manganese and cerium oxide phases obtained through XRD pattern. We can see that with increasing cerium concentration, size of iron manganese reduces due to iron upward migration cause to increase reactivity of the material.

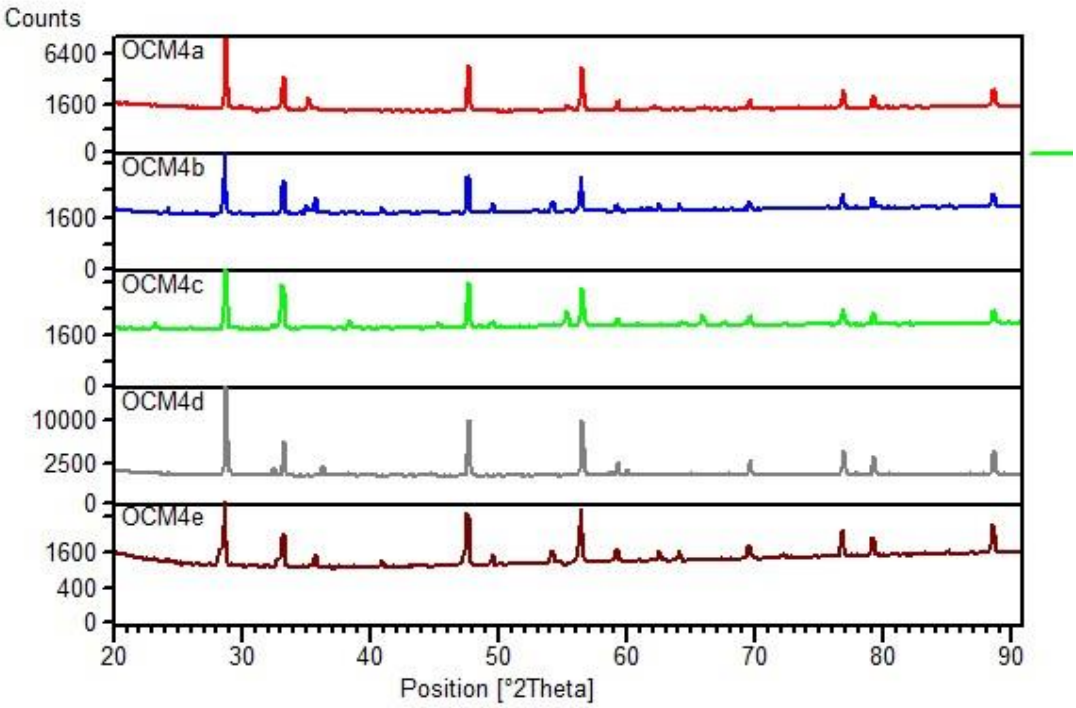

Figure 4.8 XRD spectra of material FeMnO- SDCx (x=10 wt.%, 20 wt.%)

4.5 Thermogravimetric Analysis

In the below figure shows the repeated redox cycles of iron manganese oxides with samarium doped ceria ore material behaves under different reaction times. Weight and temperature recorded as a function of time. Firstly, analyzed in the syngas presence under different temperatures from 800 to 1000℃ and time is 60 minutes set for each redox cycle. The oxidation period was small compared to reduction and inert gases was added to stabilize the reaction after oxidation. After oxidation where weight gain is faster, a stabilized period at 900℃ was performed under inert condition before the reaction of reductive gases. Due to oxygen presence in the atmosphere, weight gain in oxidation is faster than reduced weight in the reduction cause a higher kinetics in the oxidation [105].For different temperature reaction time for oxidation and reduction was same i.e., 150s and the inert period between them was for 60s. We can say that redox reaction rate not affected by temperature or independent. To ensure reproducibility the redox cycle at least 3 times was repeated. Material sample amount was chosen to be 2 to 18mg to minimize the measurement uncertainty[106]. Iron manganese oxides with the supporting material CeO which may be a non-reactive, help to maintain its structure and increases its porosity and activity[107].

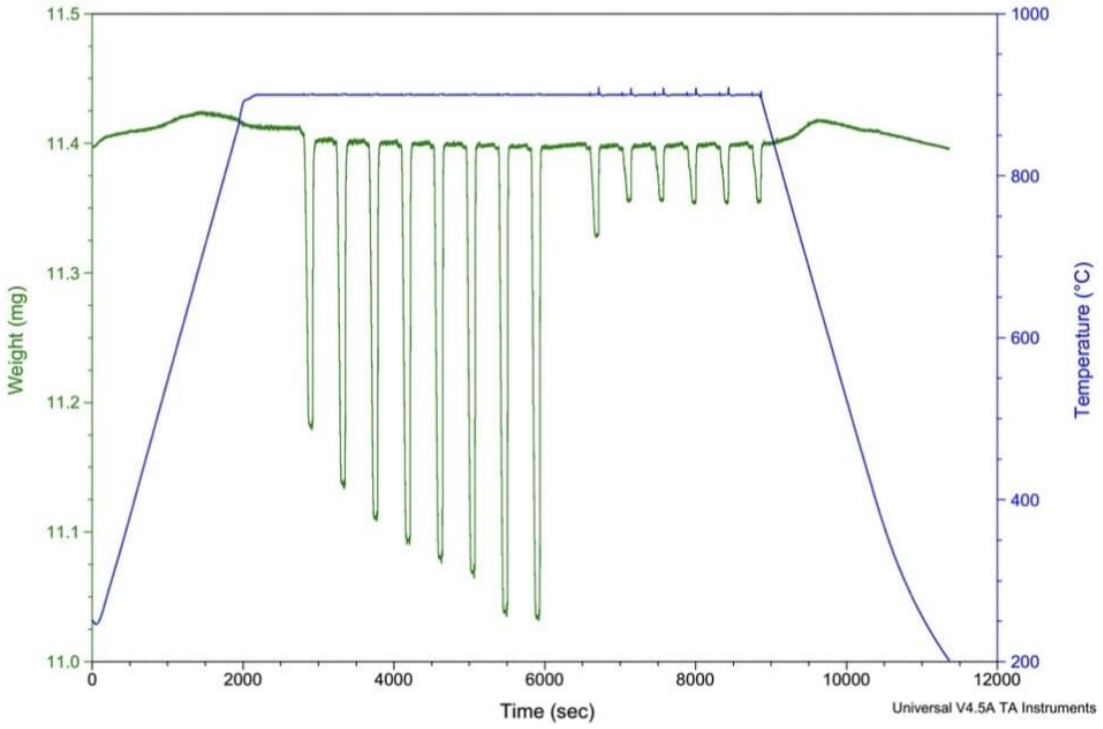

Figure 4.9 TGA Analysis of Best OC of composition(FeMnO-SDC)

The shoulder peak in the graph show a clear two step reduction caused by the CeO2 addition in the iron manganese oxides. Iron manganese oxides with SDC show low redox reactivity towards methane due to low reactivity between lattice oxygen of iron manganese and methane or high energy bond of C-H present in methane. When cerium was introduced, lattice oxygen atom of cerium form oxygen vacancies due to its activeness when iron manganese is in contact with methane. Cerium promoted the above side reaction by activating the iron ions on the surface of iron manganese oxides. Cerium also show the cubic structure when OC was in reduced form also shown in XRD analysis [108]. Oxidation time was short which indicates the hematite and iron titanium oxide presence in the material that defended our XRD results also shows their occurrence. After completing the redox cycles samples were gradually left to cool down under air inside the TGA.

Ro is the oxygen transport capacity can be calculated by

$$R_o = \frac{mo-mr}{mo}\times 100 \qquad \textbf{(21)}$$

Fractional reduction x_r:

$$x_r = \frac{mo-m}{mo-mr} \times \frac{mo-m}{Romo} \quad \textbf{(22)}$$

Fractional Oxidation x_o:

$$x_o = \frac{m-mr}{mo-mr} \times \frac{m-mr}{Romo} \quad \textbf{(23)}$$

Table 4.3: Behavior of synthesized best oxygen carrier material FexMn1-xO-SDCx (x=10 wt.%, 20 wt.%)

No: Redox Cycle	R_o	X_o	X_r
1.	6.45	0.5	0,5
2.	9.678	0.6	0.4
3.	10.32	0.67	0.32
4.	11.02	0.70	0.3
5.	12.51	0.72	0.3

4.6 Electrochemical Impedance Spectroscopy (EIS)

To study the electrochemical impedance and behavior of prepared $Fe_xMn_{1-x}O$-SDCx (x=10 wt.%, 20 wt.%) material, the frequency response was studied with the help of the Nyquist plot. Nyquist plot is the graph of the real part of impedance against imaginary part.

The device is mounted over a stainless-steel dye which is then heated first at the desired temperature of 625℃ to see the frequency response of best two $Fe_{0.2}Mn_{0.8}O$-SDCx (x=10 wt.%, 20 wt.%) samples. Figure 4.10 and 4.11 shows the Nyquist plot of the prepared sample shows a small semicircle behavior along with a tail which signs towards the presence of both ionic and electronic conductive behavior of $Fe_{0.2}Mn_{0.8}O$-SDCx (x=10 wt.%, 20 wt.%) sample. The small semicircle signifies the presence of ionic conductivity whereas the tail signifies the presence of electronic conductivity.

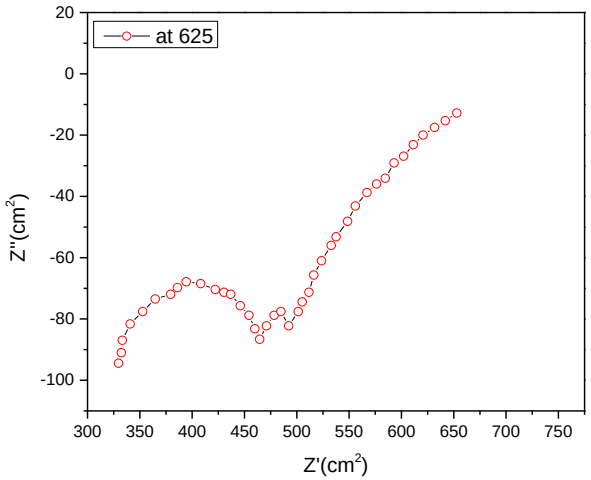

Figure 4.10 Impedance spectra of Fe0.2Mn0.8O-SDC 20 wt.% composite cathode on a SDC electrolyte

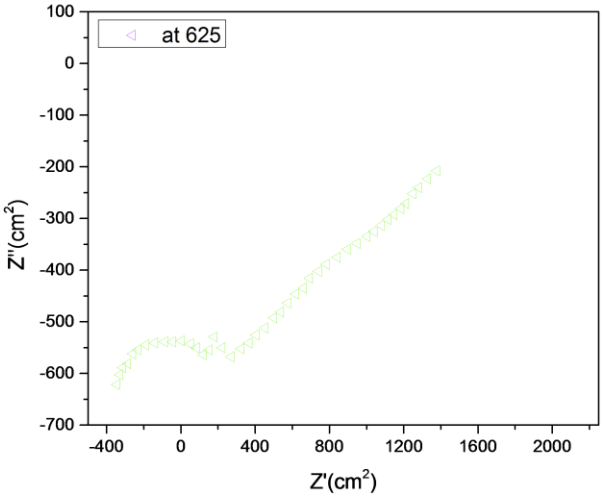

Figure 4.1Impedance spectra of Fe0.2Mn0.8O-SDC 10 wt.% composite cathode on a SDC electrolyte

Figures 4.10 and 4.11 impedance spectra show skew semicircle was recognized as originating from the $Fe_{0.2}Mn_{0.8}O$-SDCx (x=10 wt.%, 20 wt.%) interfaces in the composite cathode. The ions diffused on TPB as a result skewed semicircle formed, which is understandable for mixed ionic and electronic conductor materials but not for a pure electronic conducting material such as $Fe_{0.2}Mn_{0.8}O$. Furthermore, we can get two arcs here, one is a semi-circle and the other is a skew semicircle. We can say that the low-frequency arc is the surface/triple phase boundary reaction

and high frequency arc is the ionic conduction in the composite electrode. The semicircle diameters shrink intensely and resistance with the temperatures increasing from 450 to 650°C, which indicates that the resistance is increasing.

4.7 Conductivity Measurement

AC Conductivity is the main parameter to get better performance in the cathode material. After that EIS was performed to find the resistance of prepared cathode materials $Fe_{0.2}Mn_{0.8}O$-SDCx (x=10 wt.%, 20 wt.%) at different temperatures (550°C, 600°C, 650°C). After finding the resistance, the conductivity of materials was calculated by knowing area (A) and width of cell (L). A graph was plotted between conductivity and temperature. Figure 4.12 shows the conductivity graph of $Fe_{0.2}Mn_{0.8}O$-SDCx (x=10 wt.%, 20 wt.%) at temperatures 550°C, 600°C and 650°C. AC conductivity measurements are plotted between temperature (°C) and conductivity (Scm^{-1}). From the graph the conductivity of every material is increasing with the rise in temperature. This tendency shows semiconductor nature of material. And with increasing the value of x, conductivity is increasing. The maximum conductivity was calculated 0.13 Scm^{-1} at 650°C for $Fe_{0.2}Mn_{0.8}O$-SDCx (x=10 wt.%, 20 wt.%). It can be concluded that resistivity of materials decreases with rise in temperature resulting increase in conductivity.

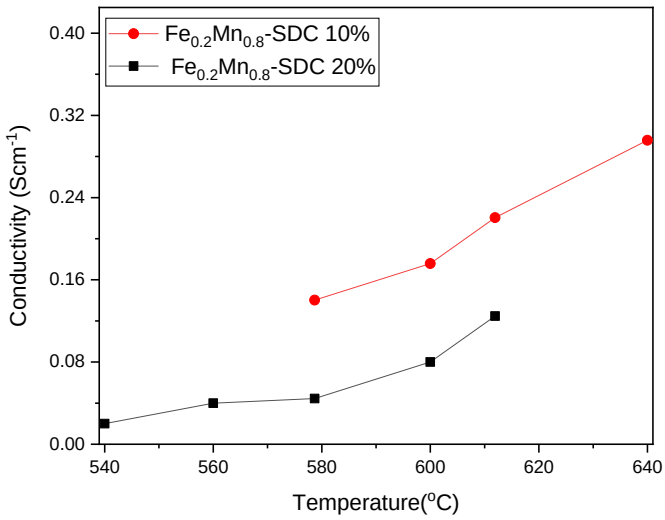

Figure 4.11 Conductivity measurement of $Fe_{0.2}Mn_{0.8}O$-SDCx (x=10 wt.%, 20 wt.%)

Conclusion

In this research work, iron manganese oxides with SDC based oxygen carriers $Fe_xMn_{1-x}O$-SDCx (x=10 wt.%, 20 wt.%) for SOFC cathode and chemical looping were synthesized by solid-state reaction method. The prepared anode materials were characterized using FTIR spectroscopy, Raman spectroscopy, X-ray Diffraction (XRD), Thermogravimetric analysis (TGA), Scanning electron microscopy (SEM). FTIR spectra represents molecular composition of prepared materials and molecular bonding. Raman spectroscopy was performed to check vibrational modes and peak shift behavior. X ray diffraction indicates the cubic crystal structure of given samples confirms that cerium addition does not change the material phase. Hematite existence in the prepared sample was identified by XRD. TGA analysis investigate the thermal properties of iron manganese material including redox cycle and oxygen carrying capacity and studies the samarium doped r55cerium effect on these properties. Scanning electron microscope analyze the morphology of the prepared material which confirms the pores on the material surface shows homogeneous and drained structure.

- From XRD reduced crystallite size of iron manganese oxide confirms its larger surface area to volume ratio for reactivity
- We can see from the TGA results that cerium addition in iron manganese increases its porosity on the surface of material and enhance its reactivity with the increasing number of redox cycles.
- Scanning electron microscope analyze the morphology of prepared material which confirms the pores on the material surface shows homogeneous and drained structure.
- The conductivity of prepared cathode materials is investigated through Electrochemical Impedance Spectroscopy (EIS) indicates semicircle diameters shrink intensely and resistance increases with the temperatures.

References

1. Holdren, J. P. (1991). Population and the energy problem. *Population and environment*, *12*(3), 231-255.
2. Raza, R., Akram, N., Javed, M. S., Rafique, A., Ullah, K., Ali, A., ... & Ahmed, R. (2016). Fuel cell technology for sustainable development in Pakistan–An over-view. *Renewable and Sustainable Energy Reviews*, *53*, 450-461.
3. Khan AN, Begum T, Sher M. Energy crisis in Pakistan causes and consequences. Abasyn J Soc Sci 2012;4:341–63.
4. Awan, K. Y., & Rashid, A. (2012). Overview of Pakistan's electricity crisis, generation-mix, and renewable energy scenarios. *International Journal of Engineering & Technology*, *1*(4), 321-334.
5. Altaf, M. H., Badrun, N. H., & Khan, M. J. H. (2014). Validation of eureka-2/rr code for analysis of pulsing parameters of triga mark ii research reactor in bangladesh. *The Nucleus*, *51*(3), 385-389.
6. Rehman, A., & Deyuan, Z. (2018). Investigating the linkage between economic growth, electricity access, energy use, and population growth in Pakistan. *Applied sciences*, *8*(12), 2442.
7. Jayaraman, T. K., & Lau, E. (2011). Oil price and economic growth in small Pacific Island countries. *Modern Economy*, *2*(2), 152-161.
8. Donnelly, L. J. (2004). Geological investigations at a high altitude, remote coal mine on the Northwest Pakistan and Afghanistan frontier, Karakoram Himalaya. *International journal of coal geology*, *60*(2-4), 117-150.
9. Chaudhry, M. A., Raza, R., & Hayat, S. A. (2009). Renewable energy technologies in Pakistan: prospects and challenges. *Renewable and Sustainable Energy Reviews*, *13*(6-7), 1657-1662.
10. Pazheri, F. R., Othman, M. F., & Malik, N. H. (2014). A review on global renewable electricity scenario. *Renewable and Sustainable Energy Reviews*, *31*, 835-845.
11. Semelsberger, T. A., Borup, R. L., & Greene, H. L. (2006). Dimethyl ether (DME) as an alternative fuel. *Journal of power sources*, *156*(2), 497-511.

12. Carrette, L., Friedrich, K. A., & Stimming, U. (2000). Fuel cells: principles, types, fuels, and applications. *ChemPhysChem*, *1*(4), 162-193.
13. Raza, R., Akram, N., Javed, M. S., Rafique, A., Ullah, K., Ali, A., ... & Ahmed, R. (2016). Fuel cell technology for sustainable development in Pakistan–An over-view. *Renewable and Sustainable Energy Reviews*, *53*, 450-461.
14. Demirbaş, A. (2006). Global renewable energy resources. *Energy sources*, *28*(8), 779-792.
15. Dincer, I. (2001). Environmental issues: Ii-potential solutions. *Energy sources*, *23*(1), 83-92.
16. Bilgen, S., Kaygusuz, K., & Sari, A. (2004). Renewable energy for a clean and sustainable future. *Energy sources*, *26*(12), 1119-1129.
17. Hu, H., Lin, Q., Zhu, Z., Liu, X., Afzal, M., He, Y., & Zhu, B. (2015). Effects of composition on the electrochemical property and cell performance of single layer fuel cell. *Journal of Power Sources*, *275*, 476-482.
18. Qureshi, M. I., Rasli, A. M., & Zaman, K. (2016). Energy crisis, greenhouse gas emissions and sectoral growth reforms: Repairing the fabricated mosaic. *Journal of Cleaner Production*, *112*, 3657-3666.
19. Alvarado-Flores, J. J., Mondragón-Sánchez, R., Avalos-Rodrıguez, M. L., Alcaraz-Vera, J. V., Rutiaga-Quinones, J. G., & Guevara-Martınez, S. J. (2021). Synthesis, characterization, and kinetic study of the Sr_2FeMoO_{6-d} double perovskite: new findings on the calcination of one of its precursors.
20. Jeong D. Jun A. Ju Y-W. Hyodo J. Shin J. Ishihara T. Structural, electrical, and electrochemical characteristics of $LnBa_{0.5}Sr_{0.5}Co_{1.5}Fe_{0.5}O_{5þd}$ (Ln¼Pr, Sm, Gd) as cathode materials in intermediate-temperature solid oxide fuel cells. Energy Technol 2017; 5:1337e43.
21. Xia, C., Mi, Y., Wang, B., Lin, B., Chen, G., & Zhu, B. (2019). Shaping triple-conducting semiconductor $BaCo_{0.4}Fe_{0.4}Zr_{0.1}Y_{0.1}O_{3-\delta}$ into an electrolyte for low-temperature solid oxide fuel cells. *Nature communications*, *10*(1), 1707.
22. Kuai, X., Yang, G., Chen, Y., Sun, H., Dai, J., Song, Y., ... & Shao, Z. (2019). Boosting the activity of $BaCo_{0.4}Fe_{0.4}Zr_{0.1}Y_{0.1}O_{3-\delta}$ perovskite for oxygen reduction reactions at low-to-intermediate temperatures through tuning B-site cation deficiency. *Advanced Energy Materials*, *9*(38), 1902384.

23. Liu, W., Zheng, J., Wang, Y., Jiang, C., Li, D., Zhong, Z., ... & Guan, W. (2020). Structure evaluation of anode-supported planar solid oxide fuel cells based on single/double-sided electrolyte (s) under redox conditions. *International Journal of Applied Ceramic Technology*, *17*(3), 1314-1321.
24. Song, Y., Chen, Y., Xu, M., Wang, W., Zhang, Y., Yang, G., ... & Shao, Z. (2020). A cobalt-free multi-phase nanocomposite as near-ideal cathode of intermediate-temperature solid oxide fuel cells developed by smart self-assembly. *Advanced Materials*, *32*(8), 1906979.
25. Zhu, Y., Zhou, W., Chen, Y., & Shao, Z. (2016). An aurivillius oxide-based cathode with excellent CO_2 tolerance for intermediate-temperature solid oxide fuel cells. *Angewandte Chemie International Edition*, *55*(31), 8988-8993.
26. Ellis, M. W., Von Spakovsky, M. R., & Nelson, D. J. (2001). Fuel cell systems: efficient, flexible energy conversion for the 21st century. *Proceedings of the IEEE*, *89*(12), 1808-1818.
27. Schlögl, R. (2016). Sustainable energy systems: the strategic role of chemical energy conversion. *Topics in Catalysis*, *59*, 772-786.
28. Clark, W. W., Rifkin, J., O'Connor, T., Swisher, J., Lipman, T., Rambach, G., ... & Team, T. (2005). Hydrogen energy stations: along the roadside to the hydrogen economy. *Utilities Policy*, *13*(1), 41-50.
29. Sharaf, O. Z., & Orhan, M. F. (2014). An overview of fuel cell technology: Fundamentals and applications. *Renewable and sustainable energy reviews*, *32*, 810-853.
30. P Panayiotou, G., A Kalogirou, S., & A Tassou, S. (2010). PEM fuel cells for energy production in solar hydrogen systems. *Recent Patents on Mechanical Engineering*, *3*(3), 226-235.
31. Singhal, S. C., & Kendall, K. (Eds.). (2003). *High-temperature solid oxide fuel cells: fundamentals, design, and applications*. Elsevier.
32. Minh, N. Q. (1993). Ceramic fuel cells. *Journal of the American Ceramic Society*, *76*(3), 563-588.
33. Minh, N. Q., & Takahashi, T. (1995). *Science and technology of ceramic fuel cells*. Elsevier.

34. Pihlatie, M. (2010). *Stability of Ni-YSZ composites for solid oxide fuel cells during reduction and re-oxidation*. VTT.
35. Nobrega, S. D., Gelin, P., Georges, S., Steil, M. C., Augusto, B. L., Noronha, F. B., & Fonseca, F. C. (2014). A fuel-flexible solid oxide fuel cell operating in gradual internal reforming. *Journal of The Electrochemical Society*, *161*(3), F354.
36. Florides, G. A., & Christodoulides, P. (2009). Global warming and carbon dioxide through sciences. *Environment international*, *35*(2), 390-401.
37. Koronaki, I. P., Prentza, L., & Papaefthimiou, V. (2015). Modeling of CO_2 capture via chemical absorption processes− An extensive literature review. *Renewable and Sustainable Energy Reviews*, *50*, 547-566.
38. Tong, A., Zeng, L., Kathe, M. V., Sridhar, D., & Fan, L. S. (2013). Application of the moving-bed chemical looping process for high methane conversion. *Energy & fuels*, *27*(8), 4119-4128.
39. Abad, A., Mattisson, T., Lyngfelt, A., & Johansson, M. (2007). The use of iron oxide as oxygen carrier in a chemical-looping reactor. *Fuel*, *86*(7-8), 1021-1035.
40. Vigoureux, M., Leffler, T., Knutsson, P., & Lind, F. (2022). Sulfur capture and release by ilmenite used as oxygen carrier in biomass combustor. *Fuel*, *309*, 121978.
41. Archer, D. (2005). Fate of fossil fuel CO_2 in geologic time. *Journal of geophysical research: Oceans*, *110*(C9).
42. Javed, K. H., Mahmud, T., & Purba, E. (2010). The CO_2 capture performance of a high-intensity vortex spray scrubber. *Chemical Engineering Journal*, *162*(2), 448-456.
43. Cho, P., Mattisson, T., & Lyngfelt, A. (2006). Defluidization conditions for a fluidized bed of iron oxide-, nickel oxide-, and manganese oxide-containing oxygen carriers for chemical-looping combustion. *Industrial & Engineering Chemistry Research*, *45*(3), 968-977.
44. Fang, H., Haibin, L., & Zengli, Z. (2009). Advancements in development of chemical-looping combustion: a review. *International Journal of Chemical Engineering*, *2009*.
45. Figueroa, J. D., Fout, T., Plasynski, S., McIlvried, H., & Srivastava, R. D. (2008). Advances in CO_2 capture technology—the US Department of Energy's Carbon Sequestration Program. *International journal of greenhouse gas control*, *2*(1), 9-20.

46. Ishida, M., Zheng, D., & Akehata, T. (1987). Evaluation of a chemical-looping-combustion power-generation system by graphic exergy analysis. *Energy*, *12*(2), 147-154.
47. Lyngfelt, A., Leckner, B., & Mattisson, T. (2001). A fluidized-bed combustion process with inherent CO_2 separation; application of chemical-looping combustion. *Chemical Engineering Science*, *56*(10), 3101-3113.
48. Berguerand, N., & Lyngfelt, A. (2008). Design and operation of a 10 kWth chemical-looping combustor for solid fuels–Testing with South African coal. *Fuel*, *87*(12), 2713-2726.
49. Lin, S. Y., Saito, T., & Hashimoto, K. (2017). Development of the three-tower chemical looping coal combustion technology. *Energy Procedia*, *114*, 414-418.
50. Ryu, H. J., Lee, D., Jo, S. H., Lee, S. Y., & Baek, J. I. (2018, October). Preliminary test results in a 0.5 MWth pressurized chemical looping combustor. In *14th Greenhouse Gas Control Technologies Conference Melbourne* (pp. 21-26).
51. Tong, A., Bayham, S., Kathe, M. V., Zeng, L., Luo, S., & Fan, L. S. (2014). Iron-based syngas chemical looping process and coal-direct chemical looping process development at Ohio State University. *Applied energy*, *113*, 1836-1845.
52. Cho, P., Mattisson, T., & Lyngfelt, A. (2004). Comparison of iron-, nickel-, copper-and manganese-based oxygen carriers for chemical-looping combustion. *Fuel*, *83*(9), 1215-1225.
53. Jerndal, E., Mattisson, T., & Lyngfelt, A. (2006). Thermal analysis of chemical-looping combustion. *Chemical Engineering Research and Design*, *84*(9), 795-806.
54. Lyngfelt, A. (2011). Oxygen carriers for chemical looping combustion-4000 h of operational experience. *Oil & Gas Science and Technology–Revue d'IFP Energies nouvelles*, *66*(2), 161-172.
55. Idziak, K., Czakiert, T., Krzywanski, J., Zylka, A., Kozlowska, M., & Nowak, W. (2020). Safety and environmental reasons for the use of Ni-, Co-, Cu-, Mn-and Fe-based oxygen carriers in CLC/CLOU applications: An overview. *Fuel*, *268*, 117245.
56. Adanez, J., Abad, A., Garcia-Labiano, F., Gayan, P., & De Diego, L. F. (2012). Progress in chemical-looping combustion and reforming technologies. *Progress in energy and combustion science*, *38*(2), 215-282.

57. Lyngfelt, A. (2015). Oxygen carriers for chemical-looping combustion. In *Calcium and chemical looping technology for power generation and carbon dioxide (CO_2) capture* (pp. 221-254). Woodhead Publishing.
58. Adánez, J., de Diego, L. F., García-Labiano, F., Gayán, P., Abad, A., & Palacios, J. M. (2004). Selection of oxygen carriers for chemical-looping combustion. *Energy & Fuels*, *18*(2), 371-377.
59. Jerndal, E., Mattisson, T., Thijs, I., Snijkers, F., & Lyngfelt, A. (2010). Investigation of NiO/NiAl2O4 oxygen carriers for chemical-looping combustion produced by spray-drying. *International Journal of Greenhouse Gas Control*, *4*(1), 23-35.
60. Mattisson, T., Järdnäs, A., & Lyngfelt, A. (2003). Reactivity of some metal oxides supported on alumina with alternating methane and oxygen application for chemical-looping combustion. *Energy & Fuels*, *17*(3), 643-651.
61. Wolf, J., Anheden, M., & Yan, J. (2005). Comparison of nickel-and iron-based oxygen carriers in chemical looping combustion for CO_2 capture in power generation. *Fuel*, *84*(7-8), 993-1006.
62. Schwebel, G. L., Filippou, D., Hudon, G., Tworkowski, M., Gipperich, A., & Krumm, W. (2014). Experimental comparison of two different ilmenites in fluidized bed and fixed bed chemical-looping combustion. *Applied energy*, *113*, 1902-1908.
63. Yu, Z., Yang, Y., Yang, S., Zhang, Q., Zhao, J., Fang, Y., ... & Guan, G. (2019). Iron-based oxygen carriers in chemical looping conversions: A review. *Carbon Resources Conversion*, *2*(1), 23-34.
64. O'Malley, K., Donat, F., Whitty, K. J., & Sohn, H. Y. (2020). Scalable preparation of bimetallic Cu/Ni-based oxygen carriers for chemical looping. *Energy & Fuels*, *34*(9), 11227-11236.
65. Siriwardane, R., Tian, H., Richards, G., Simonyi, T., & Poston, J. (2009). Chemical-looping combustion of coal with metal oxide oxygen carriers. *Energy & Fuels*, *23*(8), 3885-3892.
66. Nandy, A., Loha, C., Gu, S., Sarkar, P., Karmakar, M. K., & Chatterjee, P. K. (2016). Present status and overview of chemical looping combustion technology. *Renewable and Sustainable Energy Reviews*, *59*, 597-619.

67. Cheng, Z., Qin, L., Fan, J. A., & Fan, L. S. (2018). New insight into the development of oxygen carrier materials for chemical looping systems. *Engineering*, *4*(3), 343-351.
68. Yamaguchi, D., Tang, L., Orellana, J., Hadley, T. D., Bhattacharya, S., & Lim, K. S. (2021). Characterization of Australian ilmenite oxygen carrier during chemical looping combustion of Victorian brown coal. *Fuel Processing Technology*, *213*, 106669.
69. Nguyen, N. M., Alobaid, F., & Epple, B. (2021). Chemical looping gasification of torrefied woodchips in a bubbling fluidized bed test rig using iron-based oxygen carriers. *Renewable Energy*, *172*, 34-45.
70. Hedayati, A., Soleimanisalim, A. H., Mattisson, T., & Lyngfelt, A. (2022). Thermochemical conversion of biomass volatiles via chemical looping: Comparison of ilmenite and steel converter waste materials as oxygen carriers. *Fuel*, *313*, 122638.
71. Chen, L., Wei, G., & Liu, K. (2022). Influences of reaction and thermal conditions on microstructural evolutions of ilmenite oxygen carriers for chemical looping combustion. *Fuel Processing Technology*, *228*, 107139.
72. Zhou, Z., Li, L., Liu, X., Zhou, Z., Sun, Z., & Duan, L. (2022). Accelerated syngas generation from chemical looping CH4 reforming by using reduced ilmenite ore as catalyst. *Fuel Processing Technology*, *232*, 107270.

73. Rasool, S. (2022). *Electrochemical Interfacial Studies of Heterogeneous Catalysis for Biogas fueled Solid Oxide Fuel Cell* (Doctoral dissertation, Physics COMSATS University Islamabad Lahore Campus).
74. West, A. R. (2006). Inorganic functional materials: optimization of properties by structural and compositional control. *The Chemical Record*, *6*(4), 206-216.
75. Mogensen, M., Lybye, D., Bonanos, N., Hendriksen, P. V., & Poulsen, F. W. (2004). Factors controlling the oxide ion conductivity of fluorite and perovskite structured oxides. *Solid State Ionics*, *174*(1-4), 279-286.
76. Raman, C. V., & Krishnan, K. S. (1928). A new type of secondary radiation. *Nature*, *121*(3048), 501-502.
77. Smith, E., & Dent, G. (2019). *Modern Raman spectroscopy: a practical approach*. John Wiley & Sons.

78. Fan, M., Dai, D., & Huang, B. (2012). Fourier transform infrared spectroscopy for natural fibres. *Fourier transform-materials analysis*, *3*, 45-68.
79. Dutta, A. (2017). Fourier transform infrared spectroscopy. *Spectroscopic methods for nanomaterials characterization*, 73-93.
80. Ferraro, J. R., & Basile, L. J. (Eds.). (2012). *Fourier transform infrared spectra: applications to chemical systems*. Academic press.
81. Li, Y., Li, Z., Liu, L., & Cai, N. (2020). Measuring the fast oxidation kinetics of a manganese oxygen carrier using microfluidized bed thermogravimetric analysis. *Chemical Engineering Journal*, *385*, 123970.
82. Adánez, J., Cuadrat, A., Abad, A., Gayán, P., de Diego, L. F., & Garcia-Labiano, F. (2010). Ilmenite activation during consecutive redox cycles in chemical-looping combustion. *Energy & Fuels*, *24*(2), 1402-1413.
83. Li, Y., Wang, H., Li, W., Li, Z., & Cai, N. (2018). CO_2 gasification of a lignite char in microfluidized bed thermogravimetric analysis for chemical looping combustion and chemical looping with oxygen uncoupling. *Energy & fuels*, *33*(1), 449-459.
84. Beane, R. J. (2004). Using the scanning electron microscope for discovery-based learning in undergraduate courses. *Journal of Geoscience Education*, *52*(3), 250-253.
85. Chkirida, S., Zari, N., Achour, R., & Bouhfid, R. (2020). Effect of iron doped titanium oxide encapsulated in alginate on photocatalytic activity for the removal of dye pollutants. *RSC advances*, *10*(38), 22311-22317.
86. Chandradass, J., Nam, B., & Kim, K. H. (2009). Fine tuning of gadolinium doped ceria electrolyte nanoparticles via reverse microemulsion process. *Colloids and Surfaces A: Physicochemical and Engineering Aspects*, *348*(1-3), 130-136.
87. Darezereshki, E. (2011). One-step synthesis of hematite (α-Fe2O3) nanoparticles by direct thermal-decomposition of maghemite. *Materials Letters*, *65*(4), 642-645.
88. Mylarappa, M., Lakshmi, V. V., Mahesh, K. V., Nagaswarupa, H. P., & Raghavendra, N. (2016, September). A facile hydrothermal recovery of nano sealed MnO2 particle from waste batteries: An advanced material for electrochemical and environmental applications. In *IOP Conference Series: Materials Science and Engineering* (Vol. 149, No. 1, p. 012178). IOP Publishing.

89. Wattanathana, W., Lakkham, A., Kaewvilai, A., Koonsaeng, N., Laobuthee, A., & Veranitisagul, C. (2011). Preliminary study of Pd/CeO2 derived from cerium complexes as solid support catalysts for hydrogenation reaction in a micro-reactor. *Energy Procedia*, *9*, 568-574.
90. De Faria, D. L., Venâncio Silva, S., & De Oliveira, M. T. (1997). Raman micro spectroscopy of some iron oxides and oxyhydroxides. *Journal of Raman spectroscopy*, *28*(11), 873-878.
91. Kotenev, V. A. (2020). Raman Spectroscopy of Iron-Oxide Core-Corona Nanoparticles: Effect of Synthesis Temperature. *Protection of Metals and Physical Chemistry of Surfaces*, *56*, 1159-1167.
92. McCarty, K. F., & Boehme, D. R. (1989). A Raman study of the systems Fe3− xCrxO4 and Fe2− xCrxO3. *Journal of solid-state chemistry*, *79*(1), 19-27.
93. Chernyshova, I. V., Hochella Jr, M. F., & Madden, A. S. (2007). Size-dependent structural transformations of hematite nanoparticles. 1. Phase transition. *Physical Chemistry Chemical Physics*, *9*(14), 1736-1750.
94. Chou, H., & Fan, H. Y. (1976). Light scattering by magnons in CoO, MnO, and α− MnS. *Physical Review B*, *13*(9), 3924.
95. Mita, Y., Sakai, Y., Izaki, D., Kobayashi, M., Endo, S., & Mochizuki, S. (2001). Optical study of MnO under high pressure. *physica status solidi (b)*, *223*(1), 247-251.
96. Mironova-Ulmane, N., Kuzmin, A., & Grube, M. (2009). Raman and infrared Spectro microscopy of manganese oxides. *Journal of Alloys and Compounds*, *480*(1), 97-99.
97. Baqer, A. A., Matori, K. A., Al-Hada, N. M., Shaari, A. H., Saion, E., & Chyi, J. L. Y. (2017). Effect of polyvinylpyrrolidone on cerium oxide nanoparticle characteristics prepared by a facile heat treatment technique. *Results in physics*, *7*, 611-619.
98. Sanders, S., & Golden, T. D. (2019). Functionalization of cerium oxide nanoparticles to influence hydrophobic properties. *Langmuir*, *35*(17), 5841-5847.
99. Radhakrishnan, R., Lakshmi, D., Khan, F. A., Ramalingam, G., & Kaviyarasu, K. (2020). Biosynthesis of iron oxide nanoparticles using neem leaf cake extract and its influence in

the agronomical traits of vigna mungo plant. *Asian Journal of Nanoscience and Materials*, *3*, 38-46.

100. Dutta, A. (2017). Fourier transform infrared spectroscopy. *Spectroscopic methods for nanomaterials characterization*, 73-93.

101. Liu, X. D., Zhang, H. Y., Lu, K., & Hu, Z. Q. (1994). The lattice expansion in nanometer-sized Ni polycrystals. *Journal of Physics: Condensed Matter*, *6*(34), L497.

102. Jahagirdar, A. A., Dhananjaya, N., Monika, D. L., Kesavulu, C. R., Nagabhushana, H., Sharma, S. C., ... & Chakradhar, R. P. S. (2013). Structural, EPR, optical and magnetic properties of α-Fe2O3 nanoparticles. *Spectrochimica Acta Part A: Molecular and Biomolecular Spectroscopy*, *104*, 512-518.

103. Raghavender, A. T., Hong, N. H., Lee, K. J., Jung, M. H., Skoko, Z., Vasilevskiy, M., ... & Samantilleke, A. P. (2013). Nano-ilmenite FeTiO3: Synthesis and characterization. *Journal of magnetism and magnetic materials*, *331*, 129-132.

104. Li, Y., Li, Z., Liu, L., & Cai, N. (2020). Measuring the fast oxidation kinetics of a manganese oxygen carrier using microfluidized bed thermogravimetric analysis. *Chemical Engineering Journal*, *385*, 123970.

105. Lyngfelt, A., Johansson, M., & Mattisson, T. (2008). Chemical-looping combustion-status of development.

106. Sun, Z., Lu, D. Y., Ridha, F. N., Hughes, R. W., & Filippou, D. (2017). Enhanced performance of ilmenite modified by CeO2, ZrO2, NiO, and Mn2O3 as oxygen carriers in chemical looping combustion. *Applied Energy*, *195*, 303-315.

107. Adánez, J., Cuadrat, A., Abad, A., Gayán, P., de Diego, L. F., & Garcia-Labiano, F. (2010). Ilmenite activation during consecutive redox cycles in chemical-looping combustion. *Energy & Fuels*, *24*(2), 1402-1413.